

AD-A110 589

AEROSPACE CORP EL SEGUNDO CA VEHICLE ENGINEERING DIV
CARBON NONEQUILIBRIUM PHASE CHANGE. (U)

F/6 T/4

DEC 81 R L BAKER

F04701-81-C-0082

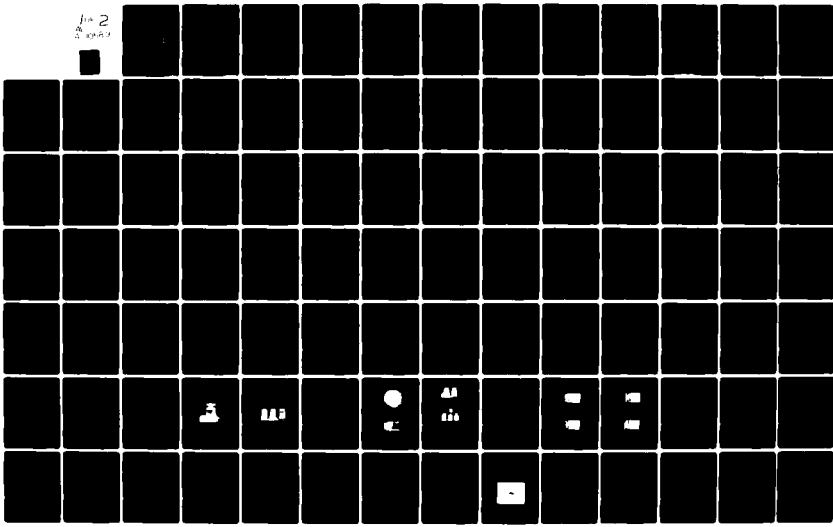
UNCLASSIFIED

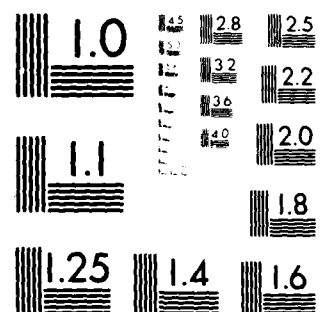
TR-0082(2728-02)-1

SD-TR-81-89

NL

File 2
12-1983





MICROCOPY RESOLUTION TEST CHART
NATIONAL BUREAU OF STANDARDS 1964 A

REPORT SD-TR-81-89

AD A110589

(12)

LEVEL II
JW

Carbon Nonequilibrium Phase Change

Prepared by

R. L. BAKER
Vehicle Engineering Division
Engineering Group
The Aerospace Corporation
El Segundo, Calif. 90245

7 December 1981

Interim Report

DTIC
ELECTED
S FEB 8 1982 D
B

APPROVED FOR PUBLIC RELEASE;
DISTRIBUTION UNLIMITED

REPRODUCTION IN WHOLE OR IN PART IS
PERMITTED FOR ANY PURPOSE OF THE
UNITED STATES GOVERNMENT.

DTIC FILE COPY

Prepared for
OFFICE OF NAVAL RESEARCH
Arlington, Va. 22217
SPACE DIVISION
AIR FORCE SYSTEMS COMMAND
Los Angeles Air Force Station
P.O. Box 92960, Worldway Postal Center
Los Angeles, Calif. 90009

This interim report was submitted by The Aerospace Corporation, El Segundo, CA 90245, under Contract No. F04701-81-C-0082 with the Space Division, Deputy for Technology, P.O. Box 92960, Worldway Postal Center, Los Angeles, CA 90009. It was reviewed and approved for The Aerospace Corporation by E. G. Hertler, Director, Aero Engineering Subdivision, and W.C. Riley, Director, Materials Sciences Laboratory. Maj Ralph R. Gajewski, SD/YLXT, was the project officer for Mission-Oriented Investigation and Experimentation (MOIE) Programs.

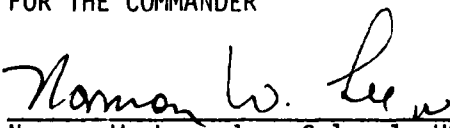
This report has been reviewed by the Public Affairs Office (PAS) and is releasable to the National Technical Information Service (NTIS). At NTIS, it will be available to the general public, including foreign nations.

This technical report has been reviewed and is approved for publication. Publication of this report does not constitute Air Force approval of the report's findings or conclusions. It is published only for the exchange and stimulation of ideas.


Ralph R. Gajewski, Major, USAF
Project Officer


Florian P. Meinhardt
Lt Col, USAF
Director of Advanced Space Development

FOR THE COMMANDER


Norman W. Lee
Norman W. Lee, Jr., Colonel, USAF
Deputy for Technology

UNCLASSIFIED

SECURITY CLASSIFICATION OF THIS PAGE (When Data Entered)

REPORT DOCUMENTATION PAGE		READ INSTRUCTIONS BEFORE COMPLETING FORM
1. REPORT NUMBER SD-TR-81-89	2. GOVT ACCESSION NO. 11-4111-539	3. RECIPIENT'S CATALOG NUMBER
4. TITLE (and Subtitle) CARBON NONEQUILIBRIUM PHASE CHANGE	5. TYPE OF REPORT & PERIOD COVERED <input checked="" type="checkbox"/> Interim Report	
	6. PERFORMING ORG. REPORT NUMBER TR-0082(2728-02)-1	
7. AUTHOR(s) R.L. Baker	8. CONTRACT OR GRANT NUMBER(s) F04701-81-C-0082	
9. PERFORMING ORGANIZATION NAME AND ADDRESS The Aerospace Corporation El Segundo, Calif. 90245	10. PROGRAM ELEMENT, PROJECT, TASK AREA & WORK UNIT NUMBERS NR-039-183-1	
11. CONTROLLING OFFICE NAME AND ADDRESS Office of Naval Research Eastern/Central Regional Office Boston, Mass. 02210	12. REPORT DATE 7 December 1981	
14. MONITORING AGENCY NAME & ADDRESS (if different from Controlling Office) Space Division Air Force Systems Command Los Angeles, Calif. 90009	13. NUMBER OF PAGES 97	
16. DISTRIBUTION STATEMENT (of this Report) Approved for public release; distribution unlimited.	15. SECURITY CLASS. (of this report) Unclassified	
17. DISTRIBUTION STATEMENT (of the abstract entered in Block 20, if different from Report)	15a. DECLASSIFICATION/DOWNGRADING SCHEDULE	
18. SUPPLEMENTARY NOTES		
19. KEY WORDS (Continue on reverse side if necessary and identify by block number) Carbon ablation Carbon thermochemistry, triple point Nonequilibrium effects		
20. ABSTRACT (Continue on reverse side if necessary and identify by block number) The need to accurately determine the thermochemical properties of carbon above 4000°K, including its melt temperature, is being addressed by an approach which seeks to determine these equilibrium properties from nonequilibrium (but steady-state) carbon ablation data. In order to do this, a non-linear model of the carbon nonequilibrium phase change process induced by high thermal radiation environments has been developed. The model allows either		

UNCLASSIFIED

SECURITY CLASSIFICATION OF THIS PAGE(When Data Entered)

19. KEY WORDS (Continued)

20. ABSTRACT (Continued)

sublimation or melting with subsequent vaporization. In addition, we have obtained, partly in collaborative work with NASA Ames, high-temperature (3500 to 4700°K), nonequilibrium carbon ablation data using laser radiation at power densities ranging from 10 to 50 kW/cm² in continuous-wave laser experiments and from 200 kW/cm² up to 4 MW/cm² in pulsed laser experiments. A discussion of model development work, the laser ablation data, and a preliminary analysis of these data are presented, along with a description of plans for more detailed data analysis to accomplish our overall objective.

UNCLASSIFIED

SECURITY CLASSIFICATION OF THIS PAGE(When Data Entered)

CONTENTS

PREFACE	9
I. INTRODUCTION	11
II. MELT LAYER MODEL	13
A. Problem Formulation	13
1. Temperature Distributions	13
2. Determination of Melt Layer Thickness	17
B. Calculated Results and Applications	22
1. Temperature Profiles	22
2. Melt Layer Thickness	23
III. NONLINEAR KNUDSEN LAYER MODELS	29
A. Background and Previous Work	29
1. Problem Description	29
2. Linearized Models	31
3. Nonlinear Models	32
B. Single Component Nonlinear Model	33
1. Problem Formulation	33
2. Calculated Results	37
3. Application to Carbon Nonequilibrium Phase Change	41

CONTENTS (Continued)

C.	Multiple Component Nonlinear Model	45
1.	Problem Formulation - Frozen Chemistry	45
2.	Problem Formulation - Equilibrium Case	48
3.	Calculated Results and Applications	49
IV.	CONTINUOUS WAVE LASER DATA	57
A.	Materials, Experimental Facility, Test Apparatus, and Instrumentation	57
1.	Materials	57
2.	Experimental Facility	57
3.	Test Apparatus and Instrumentation	59
B.	Test Planning	61
C.	Data Summary	62
D.	Preliminary Data Assessment	68
1.	Post-Test Appearance - Graphol Samples	68
2.	Post-Test Appearance - Pyrolytic Graphite Samples	75
3.	Preliminary Data Analysis	78
V.	PULSED LASER DATA	81
A.	Carbon Vaporization Experiments	81
1.	Background	81
2.	New Data Summary	82

CONTENTS (Concluded)

B.	Surface Reflectance Measurements and Spectroscopy	86
C.	Thulium Vaporization Experiments	87
D.	Preliminary Data Analysis	89
VI.	CARBON MELT TEMPERATURE	95
REFERENCES		99

Accession For	
NIST - GCR	
Type of Doc	
Title	
J. Appl. Phys.	
R:	
Distribution:	
Availability Codes	
Avail and/or Dist Special	
A	

3/4



FIGURES

1.	Steady State Melt Layer	14
2.	Liquid Layer Energy Balance	21
3.	Melt Layer Temperature Profiles	24
4.	Nondimensional Melt Layer Thickness versus α'	25
5.	Melt Layer Thickness versus Absorption Coefficient	26
6.	Melt Layer Thickness versus Radiation Intensity	28
7.	The Knudsen Layer	30
8.	Fluxes J_1 , J_2 , and J_3 in the Knudsen Layer.	35
9.	Effect of Vaporization Coefficient α on Jump Conditions Across Knudsen Layer	38
10.	Effect of γ on Jump Conditions Across Knudsen Layer	39
11.	Comparison of Linear and Nonlinear Models	40
12.	Mass Loss Rate as a Function of Solid Temperature and Edge Mach Number	43
13.	Mass Loss Rate as a Function of Radiation Intensity and Ambient Pressure	44

FIGURES (Continued)

14.	Mass Loss Rate as a Function of Radiation Intensity and Ambient Pressure	50
15.	Mass Loss Rate Behavior at Constant Solid Temperature T_s	53
16.	Mass Loss Rate Behavior at Constant Ambient Pressure p_e	54
17.	Effect of Vaporization Coefficient on Predicted Mass Loss Rates	56
18.	Sample Geometry	58
19.	Test Apparatus	60
20.	Graphol Sample, Long Duration, Low Ambient Pressure Run	70
21.	Effect of Ambient Pressure at Constant Laser Power, Graphol Samples	71
22.	Graphol Sample with Vapor-Deposited Globules	73
23.	Slotted Graphol Samples	74
24.	Pyrolytic Graphite Samples, Effect of Ambient Pressure at Constant Laser Power	76
25.	Pyrolytic Graphite Samples, Effect of Ambient Pressure at Constant Laser Power, Showing Soot Deposition	77
26.	CW Laser Ablation Data	79

FIGURES (Concluded)

- | | | |
|-----|--|----|
| 27. | Free-Jet Peak Total Pressure versus Peak Surface Temperature | 83 |
| 28. | Derived Free-Jet Total Pressure versus Peak Laser Flux for Vaporization in Argon | 84 |
| 29. | Peak Surface Temperature versus Peak Laser Flux for Vaporization in Argon | 85 |
| 30. | Comparison of Calculated and Experimental Spectra - C_2 ($\Delta v = 0$) and C_3 | 88 |
| 31. | Self-Luminous Monatomic Thulium Vapor Plume Created by Laser Heating | 90 |
| 32. | Dependence of Mass Loss Rate on Vaporization Coefficient and T_s | 92 |

TABLES

1.	Graphnol Data	63
2.	Pyrolytic Graphite Data	66

PREFACE

This work was supported by the Office of Naval Research under AF/SD Contract No. F05728-79-C-0080. The encouragement and enthusiastic support of contract monitor Dr. L.H. Peebles is gratefully acknowledged. The author also wishes to thank Dr. R.A. Meyer for his help, Dr. A.G. Whittaker and Mr. P.L. Kintner for the use of their test apparatus and dedicated assistance, Professor Gerd Rosenblatt for stimulating discussions and helpful suggestions, Mr. Alan Covington and Dr. K.A. Lincoln for their work and enthusiastic cooperation, Mr. P.G. Crowell for significant contributions in the development of the melt layer model, Dr. R.J. Bywater for his continued interest and helpful discussions concerning Knudsen layers, and Dr. W.M. Adams and Mr. R.F. Kramer for timely and efficient computer programming.

I. INTRODUCTION

The use of carbon materials in advanced thermal protection system applications requires an understanding of the thermochemistry of carbon at temperatures exceeding 4000°K ^{1,2}. Of primary importance is an accurate knowledge of the melt temperature, the species vapor pressures, and species vaporization coefficients, since these properties directly affect the energy-dissipating efficiency. At present, the uncertainty in the melt temperature of carbon is at least 600°K , and recommended thermochemical data from different investigators result in predicted total vapor pressures differing by more than an order of magnitude above 4000°K ³⁻⁵. Of equal importance is an understanding of the nonequilibrium nature of the phase change process when massive interphase mass transfer takes place such as that induced by high intensity thermal radiation.

The approach of our work^{1,2} has been to address simultaneously the needs of high-temperature carbon thermochemical property data and nonequilibrium phase change modeling. The development of a nonequilibrium phase change model first allows the interpretation of laser-induced phase change experimental data; i.e., equilibrium thermochemical property information can be

¹ "Proposal to Perform a Carbon Nonequilibrium Phase Change Research Program," The Aerospace Corporation, El Segundo, Calif., April 1979.

² "Proposal to Continue the Carbon Nonequilibrium Phase Change Research Program," The Aerospace Corporation, El Segundo, Calif., August 1979.

³ Baker, R.L., "An Irreversible Thermodynamics Model for Graphite Sublimation in Radiation Environments," Progress in Astronautics and Aeronautics: Outer Planet Heating and Thermal Protection Systems, 64, R. Viskanta (ed.), AIAA, New York, 1979, pp. 210-227.

⁴ Baker, R.L. and P.G. Crowell, "Graphite Material Ablation Performance in High Thermal Radiation Environments," Progress in Astronautics and Aeronautics: Entry Heating and Thermal Protection, 69, W. Olstad (ed.), AIAA, New York, 1980, pp. 198-221.

⁵ Baker, R.L., "Graphite Sublimation Chemistry Nonequilibrium Effects," AIAA Journal, 15, Oct. 1977, pp. 1391-1397.

obtained from a nonequilibrium experiment. After the required information has been obtained, the same model then can be utilized for design applications involving carbon materials at extreme temperatures and under nonequilibrium conditions.

Toward this end we have developed, in the past year, a nonlinear non-equilibrium model applicable to the carbon phase change process which allows either direct sublimation or melting with subsequent vaporization. This work is an extension of our earlier work involving linearized models³⁻⁵. In addition, we have obtained, partly in collaborative work with NASA Ames, high-temperature (3500 to 4700°K) carbon ablation data using laser radiation at power densities ranging from 10 to 50 kW/cm² in continuous wave laser experiments and from 200 kW/cm² up to 4 MW/cm² in pulsed laser experiments.

The major overall objective of this work is to use the model development effort, discussed in Sections II and III, to interpret the laser-induced carbon nonequilibrium phase change data, described in Sections IV and V, in such a way as to obtain the needed information, i.e., carbon species heats of formation, free energy functions, and vaporization coefficients, as well as the melt temperature of carbon. Preliminary data analyses are included as part of the continuous wave laser and pulsed laser data discussions in Sections IV and V, respectively. The melt temperature question is discussed in Section VI. Detailed analysis of these data, to obtain a critical evaluation of the validity of the JANNAF thermochemical property data and the melt temperature of carbon, is planned as part of the continuation of this work.

II. MELT LAYER MODEL

The surface boundary condition for the heat conduction into the bulk material becomes fundamentally different when a semitransparent melt layer occurs on the surface and the energy input is supplied by radiation. Thus, in order to compare experimental pulsed laser data with results predicted from the nonlinear, nonequilibrium phase change analysis described in Section III, proper accounting of this melting surface boundary condition must be made. An equivalent melt layer problem, where the energy input is supplied by a heat source or forced convection heat transfer, was described by Landau⁶ and more recently by Crowell⁷. Their approach is used below to describe the case in which simultaneous radiation absorption and thermal conduction occur in the melt layer. The problem formulation is given in Subsection II-A, and representative calculated results and applications are discussed in Subsection II-B. The model must be used in conjunction with the nonlinear Knudsen layer models described in Section III for all data analyses in which carbon melting at the surface is postulated to have occurred.

A. PROBLEM FORMULATION

1. Temperature Distributions

The problem considered is shown schematically in Fig. 1. Laser radiation of intensity I_0 impinges upon the surface. It is assumed that I_0 is sufficiently high such that melting of the material occurs, with a melt layer of thickness δ formed at the surface above the melt isotherm. Within the melt layer, laser radiation energy is simultaneously absorbed and transported by thermal conduction due to temperature gradients. Following Refs. 6. and 7, the ablation-melting process is assumed to be steady state;

⁶

Landau, H.G., "Heat Conduction in a Melting Solid," Quart. Appl. Phys. 36, Feb. 1965, pp. 462-468.

⁷

Crowell, P.G., "The Nonequilibrium Ablation of Carbon," Report No. TR-0079 (4550-76)-1, The Aerospace Corporation, El Segundo, Calif., Nov. 1978.

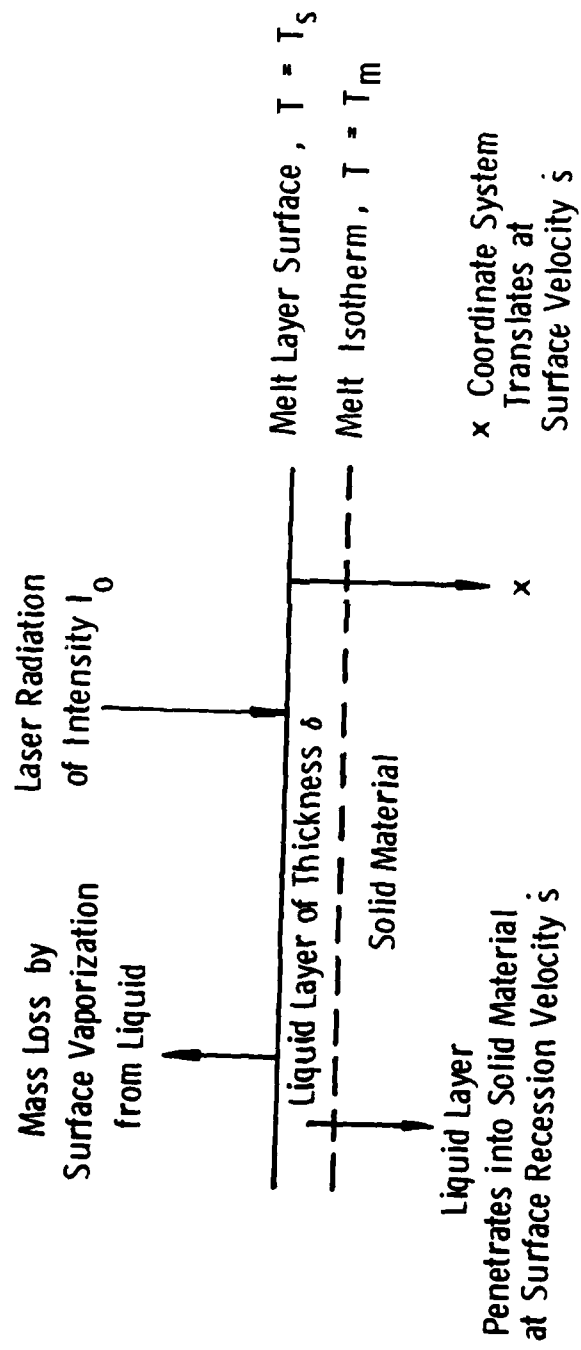


Fig. 1. Steady State Melt Layer

therefore, the melt layer surface and the melt isotherm remain separated by the distance δ , and both surfaces translate into the bulk material at the steady-state ablation rate \dot{s} , i.e., the surface velocity.

Defining one-dimensional stationary and translating coordinate systems x' and x where $x' = x + \dot{s}t$, we find the energy conservation equation for the melt layer in the stationary x' coordinate system to be

$$\rho_L C_{pL} \frac{\partial T_L}{\partial t} - \kappa I_0 e^{-\kappa(x' - \dot{s}t)} = \kappa_L \frac{\partial^2 T_L}{\partial x'^2} \quad (\text{II-1})$$

Following Landau, this equation may be transformed into the moving reference frame with coordinate x to obtain

$$\frac{d^2 T_L}{dx^2} + \frac{\dot{s}}{\sigma_L} \frac{dT_L}{dx} = - \frac{I_0}{\rho_L C_{pL} \rho_L} e^{-\kappa x} \quad (\text{II-2})$$

where σ_L is the thermal diffusivity of the liquid and κ is the spectral absorption coefficient. A time-dependent equation equivalent to Eq. (II-2) for the nonmelting case has been reported by Dabby and Paek⁸.

In the present analysis, it has been assumed that all radiation absorption within the solid takes place at the solid surface. Thus, following the procedure described above, the differential equation describing the solid temperature in the region below the melt isotherm is

$$\frac{d^2 T_S}{dx^2} + \frac{\dot{s}}{\sigma_S} \frac{dT_S}{dx} = 0 \quad (\text{II-3})$$

⁸

Dabby, F.W. and Paek, U.-C., "High-intensity Laser Induced Vaporization and Explosion of Solid Material," IEEE J. of Quantum Electronics, QE-8(2), Feb. 1972, pp. 106-111.

The boundary conditions for these second-order, ordinary differential equations are

$$\begin{aligned} \text{At } x = 0; \quad T_L &= T_s \\ \text{At } x = \delta; \quad T_L &= T_m, \quad T_S = T_m \\ \text{At } x = \infty; \quad T_S &= T_b \end{aligned} \quad (\text{II-4})$$

where T_s , T_m , and T_b are, respectively, the surface temperature of the melt layer, the melt temperature, and the bulk temperature of the solid (see Fig. 1). In all cases considered, it is assumed that $T_s > T_m \gg T_b$.

By direct application of classical linear equation solution methods and the given boundary conditions, the following expressions are obtained for the liquid and solid temperature distributions:

$$T_L = \frac{\left| T_s - T_m \right| e^{(-\dot{s}/\sigma_L)x} + T_m - T_s e^{(-\dot{s}/\sigma_L)\delta}}{\left| 1 - e^{(\dot{s}/\sigma_L)\delta} \right|}$$

$$- \frac{I_0}{\rho_L C_p L} \left[\frac{1}{\alpha' - 1} \right] \frac{\left| [1 - e^{-K\delta}] [1 - e^{(-\dot{s}/\sigma_L)x}] - [1 - e^{(-\dot{s}/\sigma_L)\delta}] [1 - e^{-Kx}] \right|}{\left| 1 - e^{-\dot{s}/\sigma_L \delta} \right|}, \quad x \leq \delta \quad (\text{II-5})$$

$$T_S = \left| T_m - T_b \right| e^{-\dot{s}(x-\delta)/\sigma_S} + T_b, \quad x \geq \delta \quad (\text{II-6})$$

The dimensionless group α' appearing in Eq. (II-5) is given by

$$\alpha'(\kappa, \sigma_L, \dot{s}) = \frac{\kappa \sigma_L}{\dot{s}} \quad (\text{II-7a})$$

2. Determination of Melt Layer Thickness δ

While Eqs. (II-6) and (II-7) give the liquid layer and solid temperature distributions, they are expressed in terms of the unknown thickness of the melt layer δ . To evaluate δ , it is necessary to supply additional information which may be obtained from the energy balance equation at the liquid-solid interface. In obtaining Eqs. (II-5) and (II-6), it has been assumed that material property values are constant. In the following, it is further assumed that $\rho_L = \rho_S = \rho$ and $C_{pL} = C_{pS} = C_p$ but not that $k_L = k_S$.

The energy balance equation at the liquid-solid interface, $x = \delta$, assuming unit absorptivity of the solid surface and neglecting emitted energy at temperature T_m , is

$$I_0 e^{-\kappa \delta} + \dot{q}_L(\delta) - \dot{q}_S(\delta) = \rho \dot{s} \Delta H_F \quad (\text{II-8})$$

In this equation, the first term represents the radiation energy transmitted through the liquid layer and absorbed at the surface of the solid. Heat conduction due to temperature gradients is given by \dot{q}_L and \dot{q}_S for the liquid and the solid, respectively. The balance of these terms supplies the energy to melt the solid at the interface with the heat of fusion given by ΔH_F . The terms $\dot{q}_L(\delta)$ and $\dot{q}_S(\delta)$ are obtained from the liquid and solid

temperature distribution Eqs. (II-5) and (II-6). Thus, differentiating these expressions, we obtain

$$\dot{q}_L(\delta) = -k_L \frac{\partial T_L}{\partial x}(\delta) = \frac{\rho C_p \dot{s} [T_s - T_m] e^{(-\dot{s}/\sigma_L)\delta}}{[1 - e^{(-\dot{s}/\sigma_L)\delta}]}$$

$$- I_0 \left[\frac{1}{\alpha' - 1} \right] \left\{ \alpha' e^{-\kappa\delta} - \frac{[1 - e^{-\kappa\delta}] e^{(-\dot{s}/\sigma_L)\delta}}{[1 - e^{(-\dot{s}/\sigma_L)\delta}]} \right\} \quad (\text{II-9})$$

$$\dot{q}_S(\delta) = \rho C_p \dot{s} [T_m - T_b] \quad (\text{II-10})$$

Substituting these expressions into Eq. (II-8), we obtain the following implicit equation for the evaluation of δ

$$A + BZ + CZ^{\alpha'} = 0 \quad (\text{II-11})$$

where $\alpha'(\kappa, \sigma_L, \dot{s})$ is given by Eq. (II-7a) and

$$A = - \frac{\rho \dot{s}}{I_0} \left[C_p (T_m - T_b) + \Delta H_f \right] \quad (\text{II-12a})$$

$$B = \frac{\rho s}{I_0} \left[C_p (T_s - T_b) + \Delta H_F \right] + \left[\frac{1}{\alpha' - 1} \right] \quad (\text{II-12b})$$

$$C = \left[\frac{-1}{\alpha' + 1} \right] \quad (\text{II-12c})$$

$$Z = e^{(-s/\sigma_L)\delta} \quad (\text{II-12d})$$

For specified input parameters, Eq. (II-11) may be solved iteratively for Z. Then δ is obtained directly from

$$\delta = - \frac{\sigma_L}{s} \ln(Z) \quad (\text{II-12e})$$

The final quantity of major interest and the main reason for carrying out the present analysis is the value of the heat conduction at the surface of the liquid layer. From Eq. (II-5) we obtain by differentiation

$$\begin{aligned} \dot{q}_L(0) &= -k_L \frac{dT_L}{dx}(0) = \frac{\rho C_p \dot{s} (T_s - T_m)}{\left[1 - e^{(-s/\sigma_L)\delta} \right]} + \\ & I_0 \left[\frac{1}{\alpha' - 1} \right] \left\{ \alpha' - \frac{\left[1 - e^{-K\delta} \right]}{\left[1 - e^{(-s/\sigma_L)\delta} \right]} \right\} \end{aligned} \quad (\text{II-13})$$

As discussed in the calculated results in Subsection II-B, this term is always negative so that radiation energy absorbed in the liquid layer is conducted back to the liquid surface where it supplies the energy required to vaporize the liquid. When the various energy transport terms are utilized as shown schematically in Fig. 2, it can be shown that in addition to the liquid-solid interface energy balance equation, (II-8), the analytic equations given here also satisfy the overall liquid layer energy balance given by

$$I_0(1 - e^{-\kappa\delta}) + \dot{q}_L(0) - \dot{q}_L(\delta) - \rho s(T_s - T_m) = 0 \quad (\text{II-14})$$

the global energy balance equation

$$I_0 - \dot{q}_T + \dot{q}_{\Delta H_F} + \dot{q}_{\Delta H_V} = 0 \quad (\text{II-15})$$

and the liquid surface energy balance

$$\dot{q}_L(0) = \dot{q}_{\Delta H_V} \quad (\text{II-16})$$

where

$$\dot{q}_T = \rho s C_p (T_s - T_b), \quad \dot{q}_{\Delta H_F} = \rho s \Delta H_F$$

$$\dot{q}_{\Delta H_V} = \rho s \left[\Delta H_V + C_{p_g} (T_g - T_s) \right] \quad (\text{II-17})$$

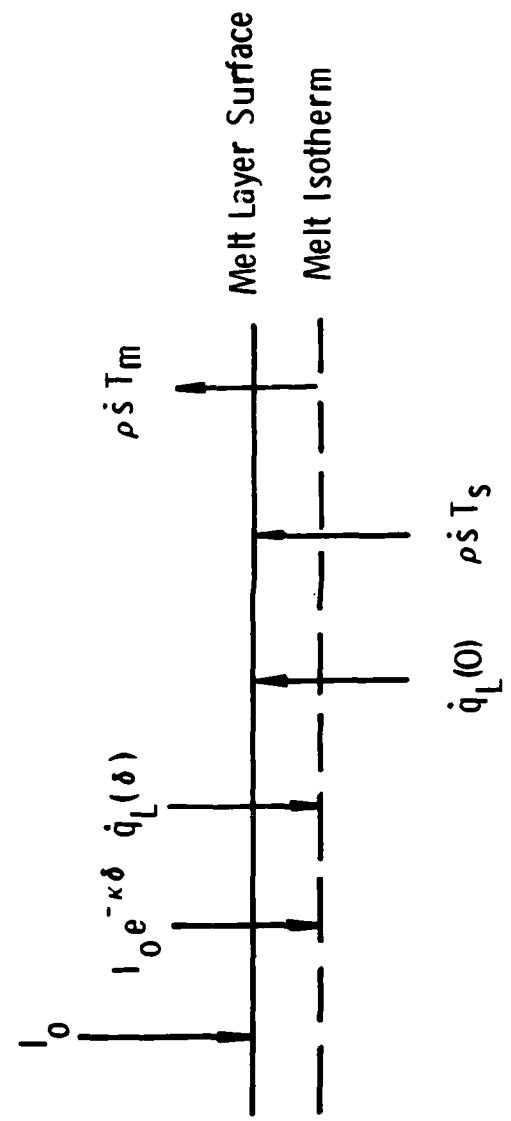


Fig. 2. Liquid Layer Energy Balance

B. CALCULATED RESULTS AND APPLICATIONS

1. Temperature Profiles

The temperature T_s in the solid below the liquid-solid interface is given by Eq. (II-6); T_s decreases monotonically and exponentially from the melt temperature T_m at the interface to the bulk solid temperature T_b far away from the interface. In contrast, the liquid melt layer temperature T_L , as given by Eq. (II-5), exhibits a maximum value within the melt layer for all positive values of α' .

Because of this maximum in the liquid temperature profile, the temperature gradient dT_L/dx is zero where $T_L = T_{L_{\max}}$, positive at $x = 0$, and negative at $x = \delta$. Thus, radiation energy absorbed within the liquid layer is conducted in two directions away from the plane within the liquid layer having temperature $T_{L_{\max}}$. At the surface $x = 0$, the heat conduction $\dot{q}_L(0)$ (Eq. (II-16)) supplies the energy required to vaporize the liquid. At the surface $x = \delta$, the heat conduction $\dot{q}_L(\delta)$ (Eq. (II-9)) supplies a portion of the energy required to melt the solid (see Eq. (II-8)).

For specified values of C_p , T_m , T_s and the effective heat of ablation $Q^* = I_0/(\rho s)$, the temperature profile $T_L = T_L(x/\delta)$ is only a function of α' . Using the effective heat of ablation Q^* , one may write α' alternatively as

$$\alpha' = \frac{\kappa \sigma_L \rho Q^*}{I_0} \quad (\text{II-7b})$$

Also, the term $I_0/(\rho_L C_p s)$ in Eq. (II-5) becomes Q^*/C_p . For an assumed melt temperature T_m of 4200°K , surface temperature T_s of 4400°K , C_p of $5/12 \text{ cal/g-}^\circ\text{K}$, and Q^* obtained directly from nonequilibrium calculations as described in Section III, the calculated liquid layer temperature profiles are shown as a

function of α' in Fig. 3. For the lower range of α' , where the predicted value of T_L becomes much larger than T_s , it is unlikely that the predicted temperature profile is achieved. More likely, in such cases, is a nucleate boiling phenomenon in the region around $T_L = T_s$ or possibly even an explosive vaporization phenomenon such as that suggested by Dabby and Paek⁸ for solids. For values of T_s other than 4400^0K , a similar dependence of the temperature profile on α' occurs.

2. Melt Layer Thickness

While the temperature profile $T_L(x/\delta)$ depends only upon α' , the liquid layer thickness δ depends upon both σ_L/s and κ . However, the dependence upon σ_L/s is given explicitly by Eq. (II-12e), and the quantity Z depends only upon α' through the implicit function represented by Eq. (II-11). Calculated values of Z using Eq. (II-11) with $T_s = 4400^0\text{K}$ and $T_m = 4200^0\text{K}$ are shown in Fig. 4 as a function of α' . Calculated results for other values of T_s ranging from 4250 to 4500^0K also have been made, and the dependence of Z on T_s is very weak.

From Fig. 4 and Eq. (II-7a), the dependence of melt layer thickness δ on spectral absorptivity κ for given σ_L/s can be readily obtained. Such results are shown in Fig. 5. For given σ_L/s , δ decreases by a factor of 30 as κ is increased two orders of magnitude. For all the calculations carried out, α' varied from 0.055 to 96.4, and the predicted liquid layer thicknesses varied by a factor of about 70. Thermal diffusivity of the liquid was varied an order of magnitude from the nominal solid carbon value of $0.93 \times 10^{-1} \text{ cm}^2/\text{sec}$ downward to $0.93 \times 10^{-2} \text{ cm}^2/\text{sec}$. The recession rate also was varied about an order of magnitude from 0.95 cm/sec to 8.6 cm/sec .

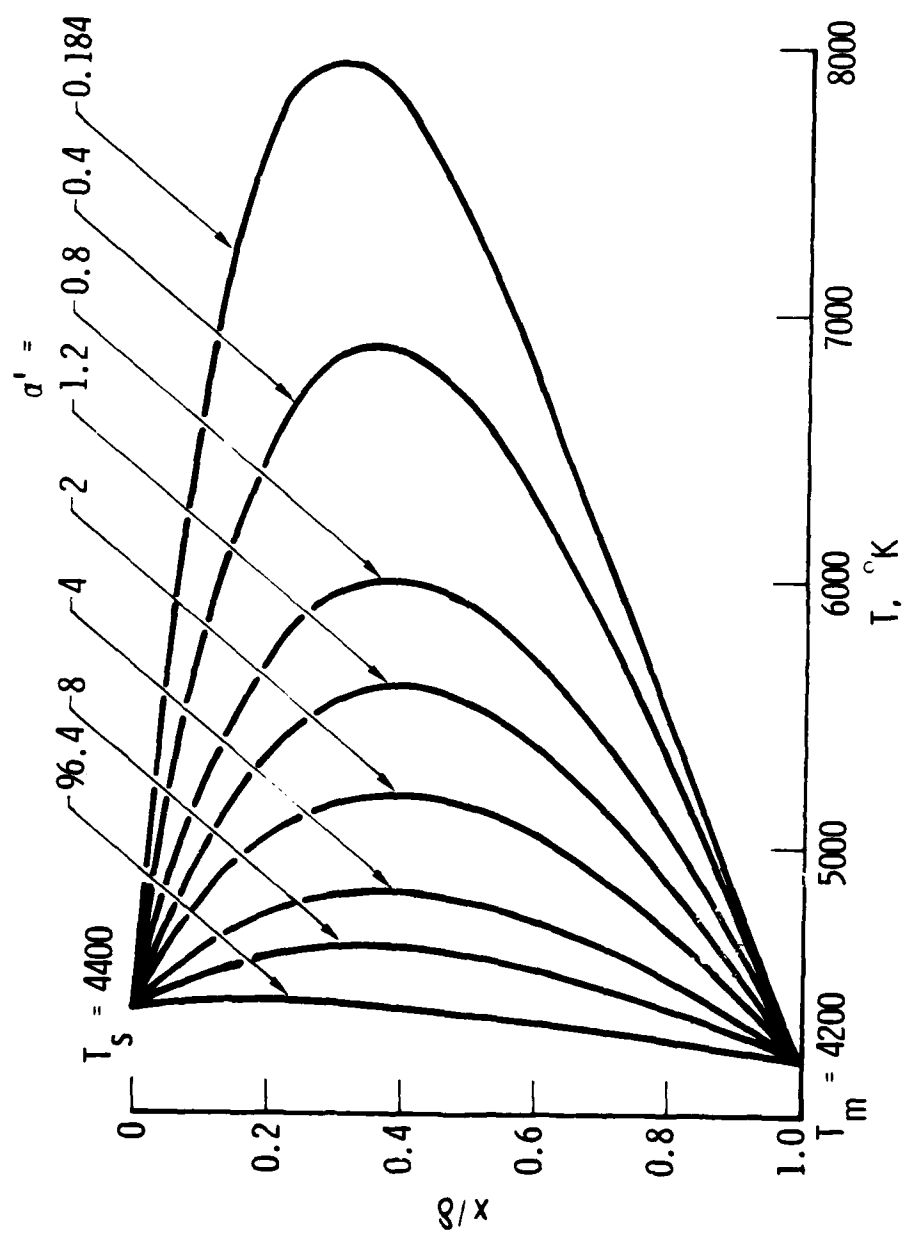


Fig. 3. Melt Layer Temperature Profiles

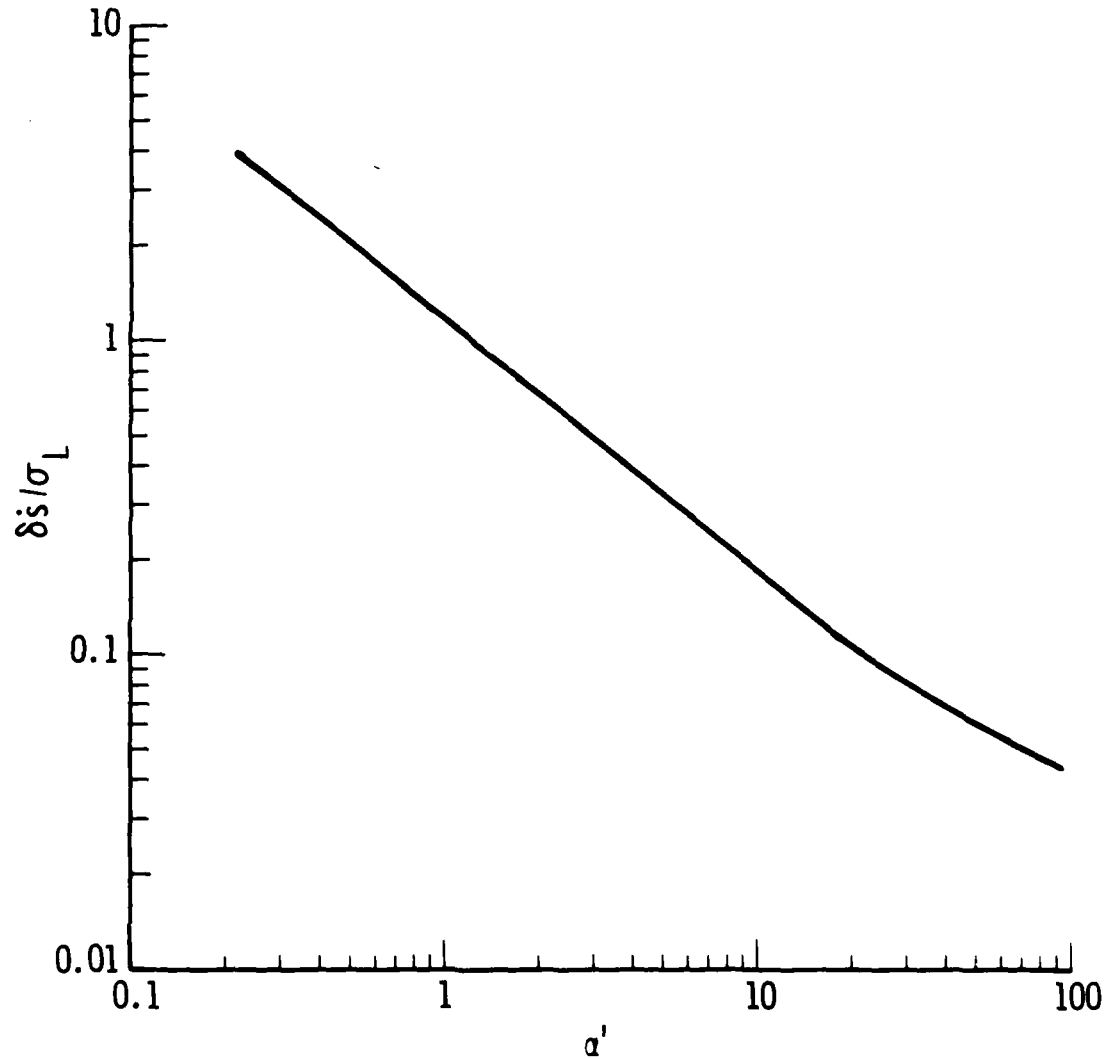


Fig. 4. Nondimensional Melt Layer Thickness versus α'

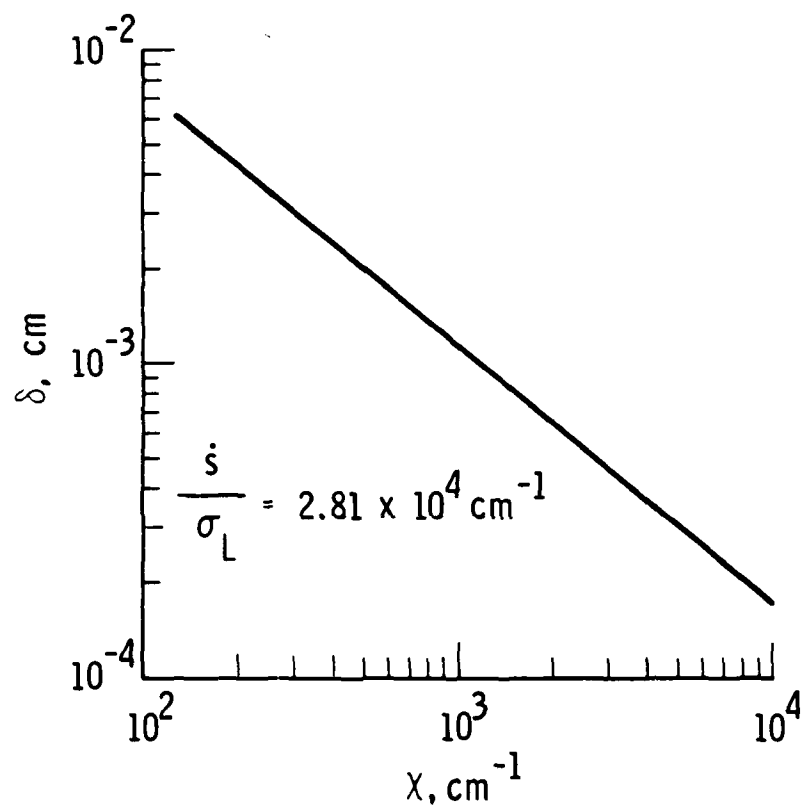


Fig. 5. Melt Layer Thickness versus Absorption Coefficient

By using an effective heat of ablation Q^* , we may express α' as a function of I_0 , i.e., Eq. (II-7b). Then, substituting $s = I_0/(\rho Q^*)$ into Eq. (II-12e), we obtain the following equation for δ as a function of I_0 :

$$\delta = - \frac{\rho Q^* \sigma_L}{I_0} \ln \left\{ z(\alpha' [I_0]) \right\} \quad (\text{II-18})$$

The dependence of δ on I_0 for $\rho Q^* = 5.36 \times 10^4 \text{ J/cm}^3$, $\kappa = 984 \text{ cm}^{-1}$, and $\sigma_L = 1.86 \times 10^{-2} \text{ cm}^2/\text{sec}$ is shown in Fig. 6. The melt layer thickness decreases about 20 percent, while I_0 increases an order of magnitude. The corresponding surface temperature T_s varied from 4250 to 5000°K .

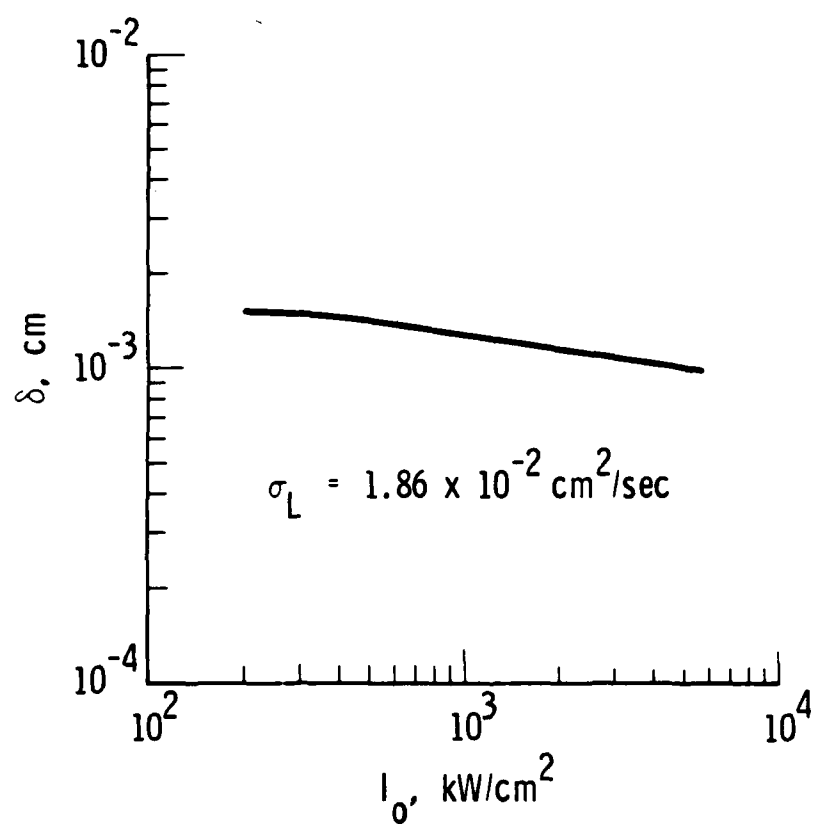


Fig. 6. Melt Layer Thickness versus Radiation Intensity

III. NONLINEAR KNUDSEN LAYER MODELS

A. BACKGROUND AND PREVIOUS WORK

1. Problem Description

A basic premise of our work on this contract since its inception has been that carbon high-temperature (3500 to 4500°K) equilibrium thermochemical properties, i.e., species vapor pressures and melt temperature, can be determined from nonequilibrium phase change laser heating experiments^{1,2}. The success of such an approach is dependent upon modeling non-equilibrium behavior in the Knudsen layer in order to interpret laser heating experiments in terms of equilibrium properties.

The essential details of the problem are illustrated in Fig. 7. The Knudsen layer is a thin region (the order of a few mean free paths in thickness) immediately above the subliming or vaporizing carbon surface, where non-equilibrium gas dynamic and chemical rate processes occur which determine the change in the carbon vapor state as it moves away from the ablating surface. Since macroscopic temperature, pressure, and species concentration measurements can only be made, at the present time, at the outer edge of the Knudsen layer, a Knudsen layer model provides a link between these measurable macroscopic variables and the equilibrium (saturation) thermodynamic properties of the carbon vapor at the solid (or liquid) surface. Consideration of the Knudsen layer becomes of first order importance for phase change problems in which the vapor pressure of the vaporizing or subliming material becomes greater than the ambient pressure³⁻⁵. This occurs typically in laser-induced phase change processes.

The basic output of a Knudsen layer analysis provides the "jump" conditions across the layer and thus relates the gas-dynamic properties at the Knudsen layer edge to equilibrium thermochemical properties of the solid or

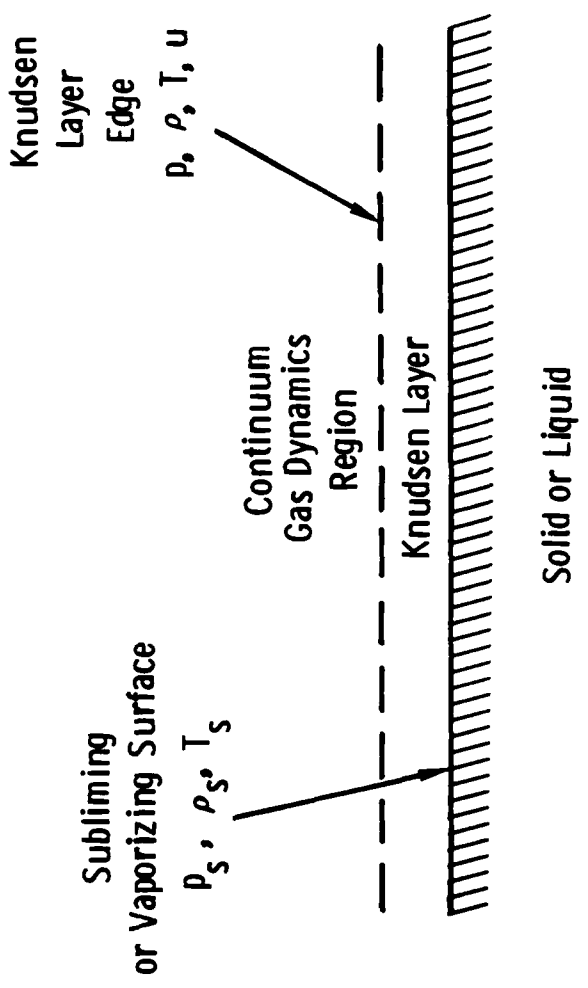


Fig. 7. The Knudsen Layer

liquid. These jump conditions have been described as being analogous to the Rankine-Hugoniot jump conditions for a normal gas-dynamic shock wave^{9,10}. However, some important distinctions must be kept in mind when speaking of such an analogy. First, a shock wave is a compression region, and a Knudsen layer is an expansion region. The most important difference is that a shock wave may be described mathematically by continuum hydrodynamic equations, unlike a Knudsen layer. The reason for this is that the velocity distribution function across a Knudsen layer is strongly nonequilibrium or non-Maxwellian. In fact, the Knudsen layer edge is defined as the location at which the velocity distribution function becomes near equilibrium. Thus, the irreversible phenomena which determine the entropy production across a shock wave and across a Knudsen layer are somewhat different.

2. Linearized Models

Most Knudsen layer analyses carried out by early investigators neglected the momentum equation, and sometimes also the energy equation, and retained only those terms which were linear in the jump conditions. An excellent summary of approaches utilizing linearized equations is given by Wiechert¹¹.

Baker⁴ adapted one of the linearized models, which utilized a non-equilibrium thermodynamics approach¹², to the carbon phase change system by assuming that carbon vapor is made up of species C₃ molecules only. More

⁹ Ytrehus, T., "Theory and Experiments on Gas Kinetics in Evaporation," Progress in Astronautics and Aeronautics: Rarefied Gas Dynamics, 51(II), J.L. Potter (ed.), AIAA, New York, 1977, pp. 1197-1212.

¹⁰ Knight, C.J., "Theoretical Modeling of Rapid Surface Vaporization with Back-Pressure," AIAA Paper 78-1220, July 1978.

¹¹ Weichert, H., "Boundary Conditions for the Liquid-Vapor Interface of Helium II," J. Phys. C: Solid State Phys., 9, 1976, pp. 553-569.

¹² Bornhorst, W.J. and G.N. Hatsopoulos, "Analysis of a Phase Change by the Methods of Irreversible Thermodynamics," Journal of Applied Mechanics, 34, Dec. 1967, pp. 840-846.

recently, this work, retaining linearized equations, was extended to include carbon species C_1 through C_5 and to consider the bounding cases of frozen and equilibrium chemistry in the Knudsen layer⁵. Comparison of calculated results using this model with pulsed laser graphite ablation data⁵ led to the tentative conclusions that carbon melting may have occurred at about 4250°K, and that the JANNAF carbon species C_3 thermochemical properties¹³ may not be correct.

3. Nonlinear Models

Recently, Knudsen layer models retaining nonlinear terms in the mass, momentum, and energy conservation equations, which determine the jumps in intensive variables across the layer, have been reported^{9,10}. This work appears to be based upon the earlier pioneering work of Anisimov¹⁴. Analytical work carried out during the past contract year has consisted of extending our previous linearized models^{4,5} by retaining all nonlinear terms in the balance equations. Initial work consisted of extending the Anisimov equations to include arbitrary values of the vaporization coefficient α and the specific heat ratio γ . Anisimov's results were for $\alpha = 1.0$ and $\gamma = 5/3$. Details of this analysis and calculated results are given in Subsection III-B. This work represents extension of our previous linearized model for a single component system to include nonlinear effects. In Subsection III-C, nonlinear balance equations are derived considering multiple species and the bounding cases of frozen and equilibrium chemistry in the Knudsen layer. This work represents extension of our previous linearized multiple species model to include nonlinear effects. Calculated results for this model also are given.

¹³

JANNAF Thermochemical Tables, National Bureau of Standards, NBS-37, June 1971.

¹⁴

Anisimov, S.I., "Vaporization of Metal Absorbing Laser Radiation," Soviet Physics JETP, 27(1), 1968, pp. 182-183.

B. SINGLE COMPONENT NONLINEAR MODEL

1. Problem Formulation

Following the approach of Anisimov¹⁴, as extended by Knight¹⁰ to include rotational degrees of freedom of the molecules, the conservation equations of mass momentum and energy for the Knudsen layer shown in Fig. 7 are

$$\rho u = \alpha \rho_s \sqrt{\frac{RT_s}{2\pi}} + \alpha \beta \rho \sqrt{\frac{RT}{2\pi}} \left[\pi^{1/2} m \operatorname{erfc}(m) - e^{-m^2} \right] \quad (\text{III-1})$$

$$\rho(u^2 + RT) = \frac{1}{2} \alpha \rho_s RT_s + (2-\alpha) \beta \rho RT \left[\left(m^2 + \frac{1}{2} \right) \operatorname{erfc}(m) - \frac{m}{\pi^{1/2}} e^{-m^2} \right] \quad (\text{III-2})$$

$$\begin{aligned} \rho u \left(\frac{5}{2} RT + \frac{1}{2} u^2 \right) &= \alpha \rho_s \sqrt{\frac{RT_s}{2\pi}} \left[2RT_s + G(\gamma)R(T_s - T) \right] \\ &+ \alpha \beta \rho RT \sqrt{\frac{RT}{2\pi}} \left[m \left(m^2 + \frac{5}{2} \right) \pi^{1/2} \operatorname{erfc}(m) - (m^2 + 2)e^{-m^2} \right] \end{aligned} \quad (\text{III-3})$$

where $G(\gamma) = (5-3\gamma)/(2(\gamma-1))$. For a vaporization coefficient α of unity, these equations reduce identically to those given by Knight. The velocity distribution functions assumed in obtaining these equations are:

For the continuum flow at the edge of the Knudsen layer

$$f_3 = \rho (2\pi RT)^{-3/2} \exp \left[-\frac{(\xi-u)^2 + \eta^2 + \zeta^2}{2RT} \right] \quad (\text{III-4a})$$

For the saturated vapor (subscript s) molecules entering the vapor phase from the solid or liquid

$$f_1 = \rho_s (2\pi RT_s)^{-3/2} \exp \left[-\frac{\xi^2 + \eta^2 + \zeta^2}{2RT_s} \right], \quad \xi > 0 \quad (\text{III-4b})$$

For the molecules entering the solid phase or reflecting back into the vapor phase from the vapor phase

$$f_2 = \beta f_3, \quad \xi < 0 \quad (\text{III-4c})$$

The contributions of the velocity distribution functions f_1 , f_2 , and f_3 to corresponding fluxes J_1 , J_2 , and J_3 in the conservation equations at the interface are illustrated in Fig. 8 for arbitrary values of the vaporization and condensation coefficients. In obtaining Eqs. (III-1) through (III-3), it has been assumed that the condensation coefficient α_c is identically equal to the vaporization coefficient α_v , since this is known to hold near equilibrium; thus, $\alpha = \alpha_c = \alpha_v$.

Equations (III-1) through (III-3) may be algebraically manipulated to obtain analytical expressions for T/T_s , ρ/ρ_s , and β as functions of $m = u/\sqrt{2RT}$ or Mach number $M = \sqrt{(2/\gamma)m}$. Carrying out the somewhat tedious algebra, we obtain

$$A(\gamma, \alpha, m) \frac{T}{T_s} + B(\gamma, \alpha, m) \sqrt{\frac{T}{T_s}} - 1 = 0 \quad (\text{III-5a})$$

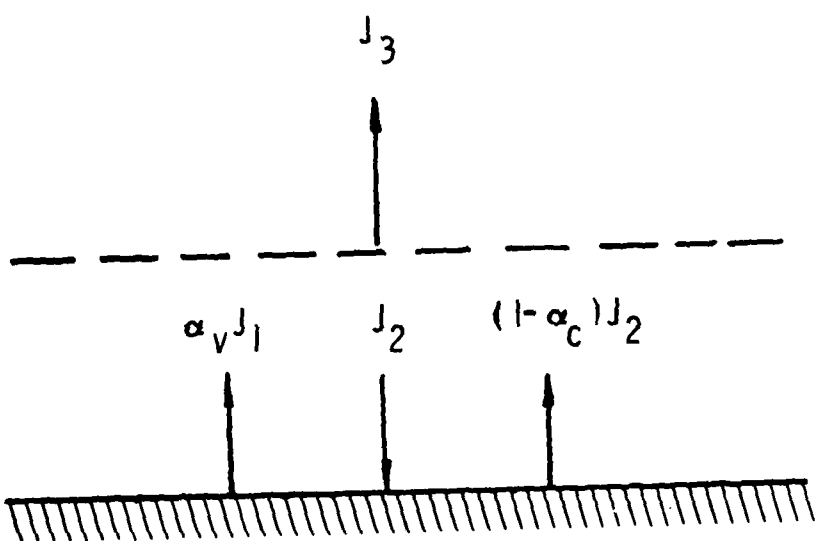


Fig. 8. Fluxes J_1 , J_2 , and J_3 in the Knudsen Layer

$$\frac{\rho}{\rho_s} = \varphi(\alpha, m) \left\{ (2-\alpha) \left[\left(m^2 + \frac{1}{2} \right) \operatorname{erfc}(m) e^{m^2} - m \pi^{-1/2} \right] \sqrt{\frac{T_s}{T}} + \frac{\alpha}{2} \left[1 - \pi^{1/2} m \operatorname{erfc}(m) e^{m^2} \right] \frac{T_s}{T} \right\} \quad (\text{III-5b})$$

$$\beta = \varphi(\alpha, m) \left[(2m^2 + 1) - m \pi^{1/2} \sqrt{\frac{T_s}{T}} \right] e^{m^2} \frac{\rho_s}{\rho} \sqrt{\frac{T_s}{T}} \quad (\text{III-5c})$$

where

$$\varphi(\alpha, m) = 1 - \frac{4(1-\alpha)}{\alpha} \left[m^2 - \pi^{1/2} m \left(m^2 + \frac{1}{2} \right) \operatorname{erf}(m) e^{m^2} \right]$$

$$A(\gamma, \alpha, m) = \left\{ 5 + 4G(\gamma) - \varphi(\alpha, m) + 2m^2 \left[1 - \varphi(\alpha, m) \right] \right\} \frac{\gamma-1}{\gamma+1}$$

$$B(\gamma, \alpha, m) = \pi^{1/2} \frac{\gamma-1}{\gamma+1} m \varphi(\alpha, m)$$

It can be easily shown that for $\alpha = 1$ and $\gamma = 5/3$, Eqs. (III-5) reduce to those given by Knight. Note that although Knight¹⁰ wrote his conservation equations for arbitrary values of γ , his expressions for T/T_s , ρ/ρ_s , and β are valid only for $\gamma = 5/3$.

2. Calculated Results

For specified values of the vaporization coefficient α and the ratio of specific heats γ , Eqs. (III-5) may be readily solved to obtain T/T_s and ρ/ρ_s as functions of the Mach number at the edge of the Knudsen layer $M = (\sqrt{2/\gamma})m$. The pressure ratio p/p_s and the mass flux ratio $\rho u / [\rho_s \sqrt{RT_s/2\pi}]$ then may be obtained from

$$\frac{p}{p_s} = \frac{\rho}{\rho_s} \frac{T}{T_s} \quad (\text{III-6a})$$

$$\frac{\dot{m}}{\dot{m}_s} = \frac{\rho u}{\rho_s \sqrt{\frac{RT_s}{2\pi}}} = 2\pi^{1/2} m \frac{\rho}{\rho_s} \sqrt{\frac{T}{T_s}} \quad (\text{III-6b})$$

To a first approximation, the carbon vapor phase may be assumed to consist of species C_3 molecules only. Then, for ideal gas behavior the γ is equal to 9/7. Calculated temperature, density, pressure, and mass flux ratios as a function of Mach number for $\gamma = 9/7$ and vaporization coefficients of 1.0, 0.6, and 0.2 are shown in Fig. 9. The effect of vaporization coefficient on the temperature ratio is minimal. However, much larger effects are seen in the density, pressure, and mass flux ratios. For these latter ratios, a decrease in the vaporization coefficient from 1.0 to 0.2 significantly decreases the Knudsen layer edge quantity relative to the reference saturation value of that quantity. Particularly noticeable are the large drops in the density and pressure ratios for $\alpha = 0.2$ between Knudsen layer edge Mach numbers M of 0 and 0.1 and the very flat mass flux ratio, again for $\alpha = 0.2$, above $M = 0.4$.

The effect of the ratio of specific heats γ for unit vaporization coefficient α are illustrated in Fig. 10. The effect is relatively weak for all the ratios, especially the density ratio. In Fig. 11, predicted results from

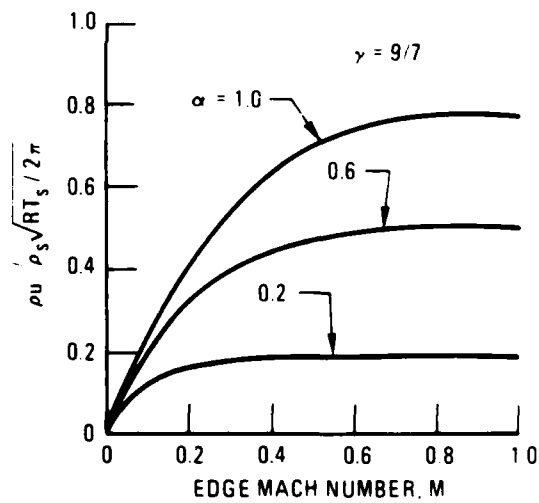
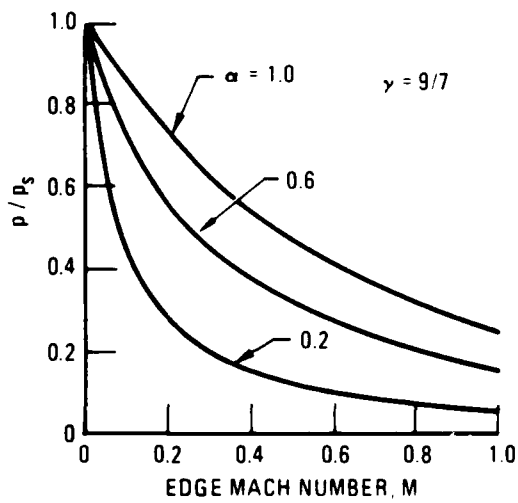
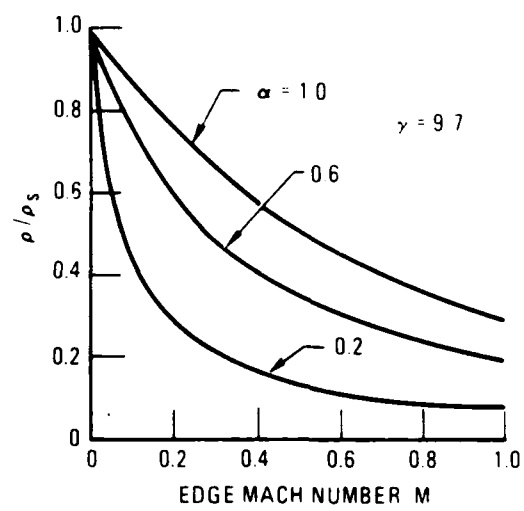
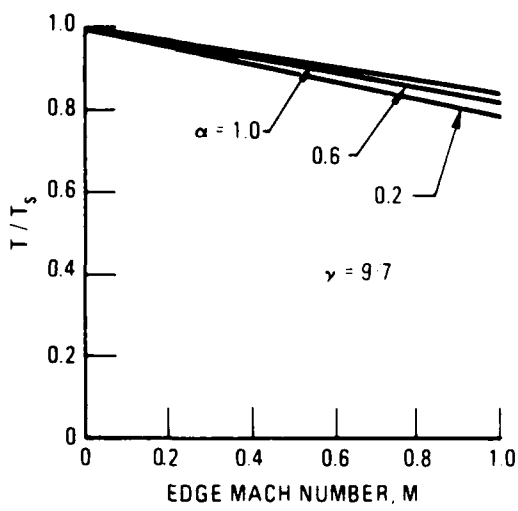


Fig. 9. Effect of Vaporization Coefficient α on Jump Conditions Across Knudsen Layer

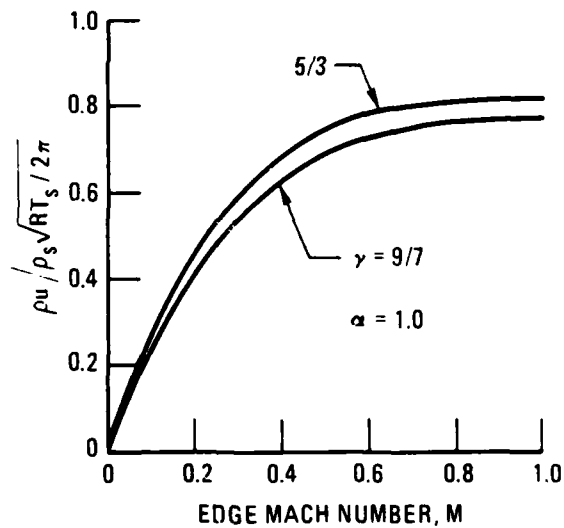
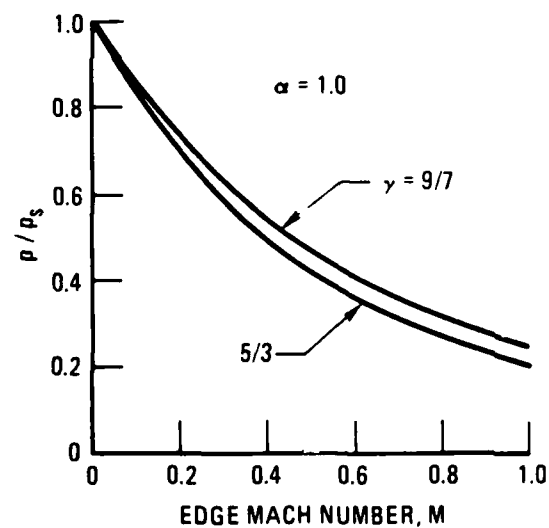
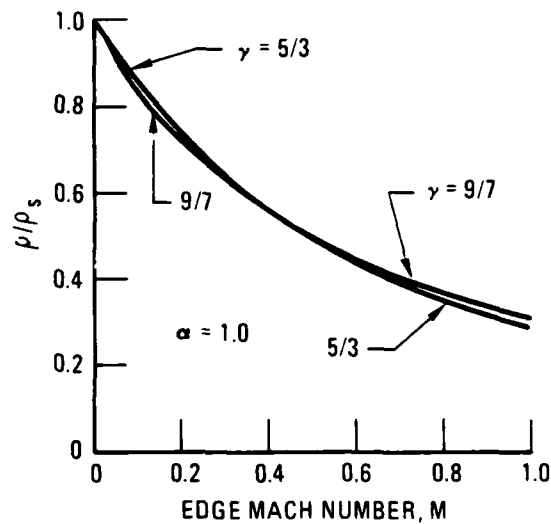
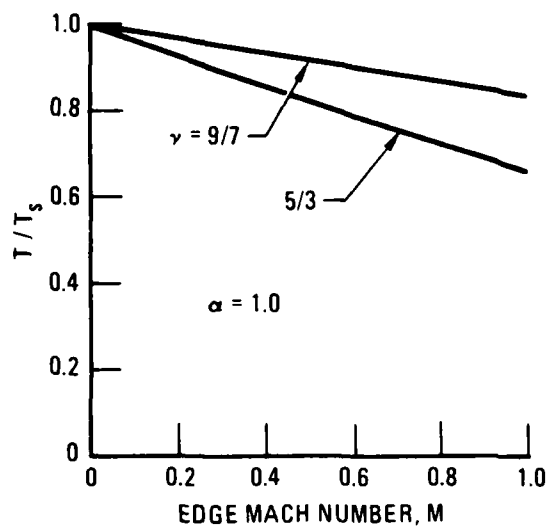


Fig. 10. Effect of γ on Jump Conditions Across Knudsen Layer

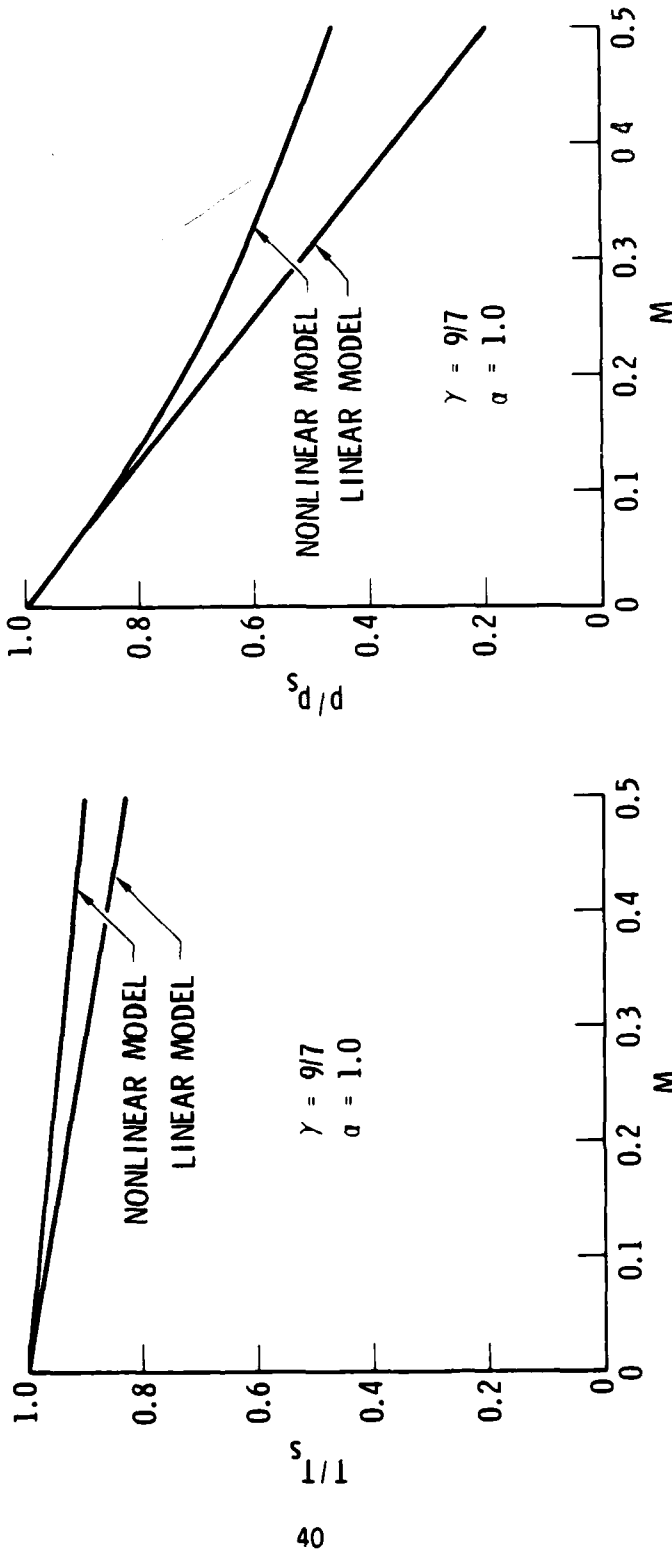


Fig. 11. Comparison of Linear and Nonlinear Models

our earlier linearized model³ and the present nonlinear model for $\gamma = 9/7$ and $\alpha = 1.0$ are compared. The temperature ratio calculated using the linear model lies below that predicted by the nonlinear model, but the error is less than eight percent even for a Knudsen layer edge Mach number M of 0.5. The pressure ratio predicted by the linear model also lies below that of the nonlinear model. However, in this case the error is about 16 percent for $M = 0.3$ and increases dramatically as M increases further.

3. Application to Carbon Nonequilibrium Phase Change

The results presented above may be easily applied to carbon nonequilibrium phase change analyses if it is assumed that the carbon vapor is made up of a single component, e.g., carbon species C₃. Alternatively, one could assign gross properties to the vapor, i.e., average molecular weight, mean values of heat of formation, free energy, vaporization coefficient, and so forth.

The calculations are closed in the same way previously discussed using the linearized model^{4,5}. Equations (III-5a) through (III-6b) or Figs. 9 and 10 provide the jump conditions across the Knudsen layer, i.e., the ratio of Knudsen layer edge quantities to those in the saturated vapor at the surface temperature, as a function of Mach number.

To calculate the mass loss rate $\dot{m} = \rho u$ for specified values of the ambient pressure p_e and input radiation heat flux I_0 , the above equations must be solved together with the surface energy balance equation. For steady-state ablation, this equation is

$$I_0 - \dot{m} [h(T, p) - c_p T_b] - \sigma \epsilon T_s^4 = 0 \quad (\text{III-7})$$

Assuming that the carbon vapor is made up of species C_3 molecules, the mass loss rate \dot{m} can be expressed using Eq. (III-6b) solely as a function of surface temperature T_s and Mach number, i.e.,

$$\dot{m} = 266 \frac{\dot{m}}{m_s} (M) \frac{p_{s_3}(T_s)}{T_s^{1/2}} \quad (\text{III-8})$$

For \dot{m} in $\text{g/cm}^2\text{-sec}$, the carbon species C_3 vapor pressure p_{s_3} should be in atmospheres and the surface temperature T_s in degrees Kelvin.

Calculation of \dot{m} thus reduces to the following iterative procedure:

- a. Guess T_s .
- b. Calculate $p_s(T_s)$ and $p/p_s = p_e/p_s$.
- c. Determine the Mach number from Fig. 9 or from Eqs. (III-6a), (III-5a), and (III-5b).
- d. For guessed T_s and calculated M , determine \dot{m} from Eq. (III-8).
- e. For temperature T obtained from Eq. (III-5a), calculate the enthalpy of the vapor at the edge of the Knudsen layer $h = h(T, p_e)$. Using this value of h , check the surface energy balance, Eq. (III-7), for the specified value of I_o .
- f. If Eq. (III-7) is not satisfied, guess a new value of T_s and return to step a.

Calculated results from Eq. (III-8) for Mach numbers of 0.2, 0.4, 0.6, 0.8, and 1.0 are shown in Fig. 12. Thus, utilizing Figs. 9 through 12, the iterative solution procedure above can easily be carried out. Alternatively, the equations discussed above can be used to calculate lines of constant I_o and constant p_e in the \dot{m} versus $1/T_s$ plane. Then, the entire iterative procedure discussed above is replaced by a single figure. The results of such calculations for the present model are shown in Fig. 13. From this figure for

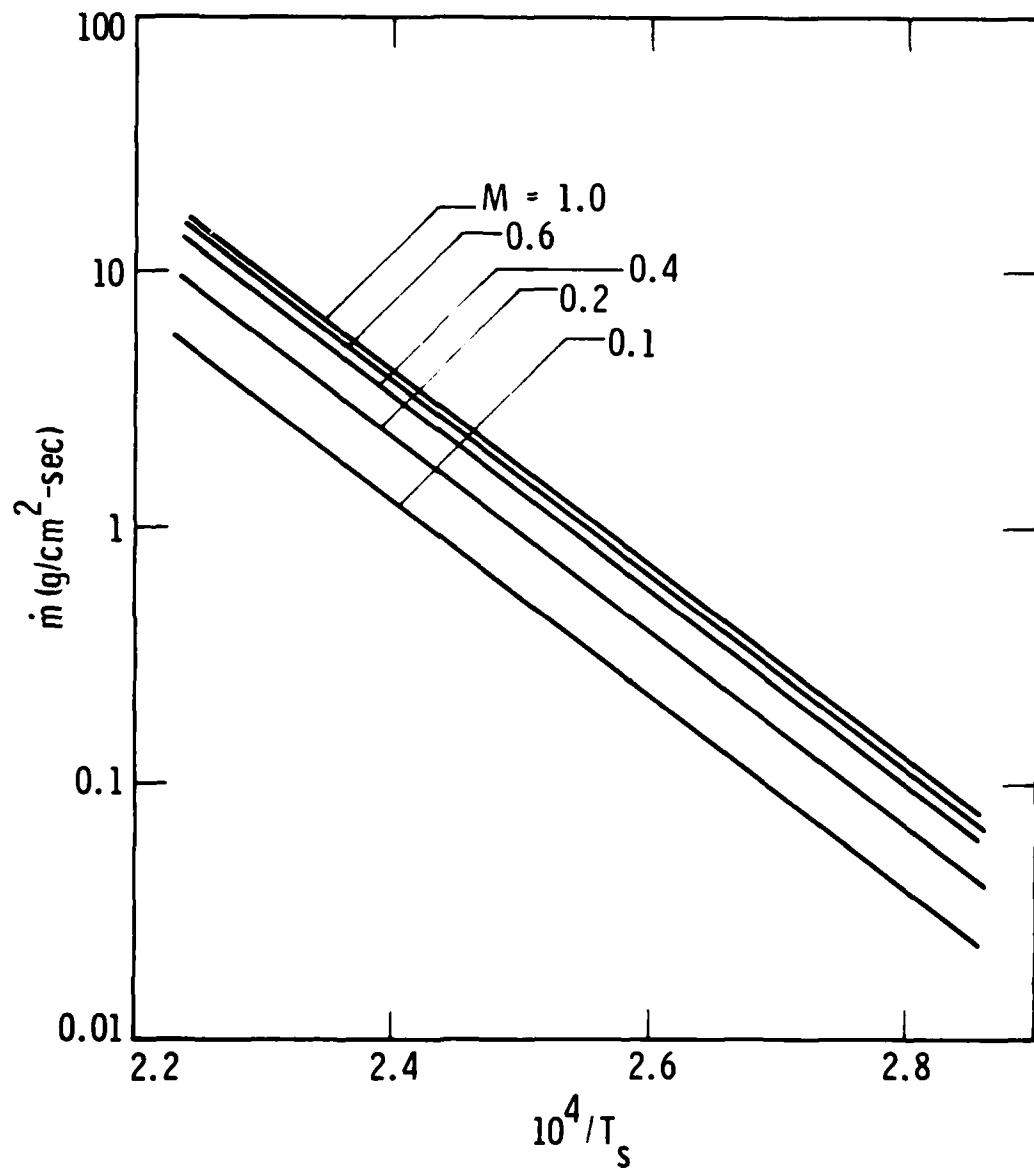


Fig. 12. Mass Loss Rate as a Function of Solid Temperature and Edge Mach Number

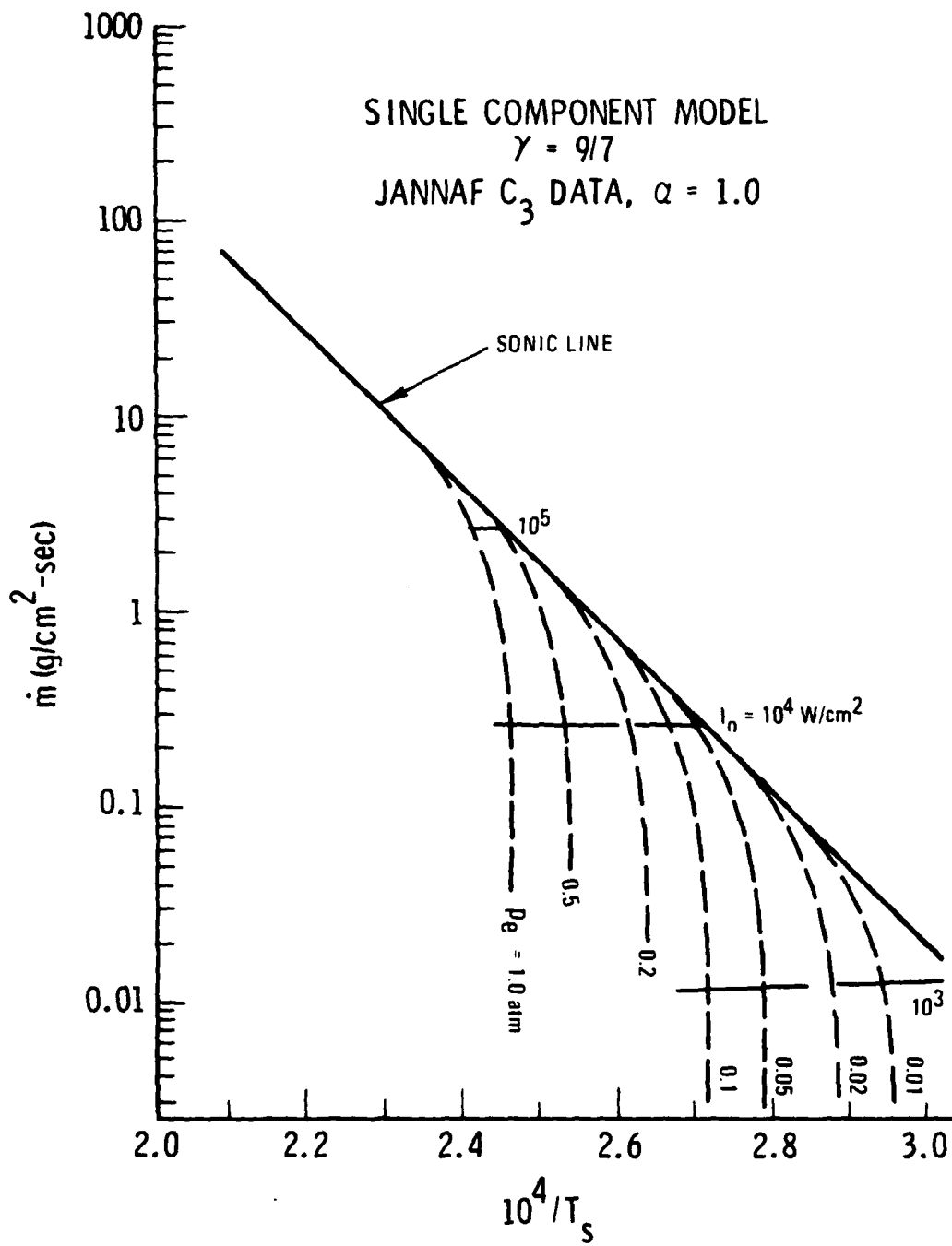


Fig. 13. Mass Loss Rate as a Function of Radiation Intensity and Ambient Pressure

specified I_0 and p_e , the mass loss rate \dot{m} and the surface temperature T_s can be obtained directly by interpolation between plotted values of I_0 and p_e .

C. MULTIPLE COMPONENT NONLINEAR MODEL

1. Problem Formulation - Frozen Chemistry

The mass, momentum, and energy conservations equations (III-1) through (III-3), when generalized to allow for more than one species in the vapor phase, become for n species

$$\rho_i u_i = \alpha_i \sqrt{\frac{R}{2\pi M_i}} \left\{ \rho_{s_i} \sqrt{T_s} + \beta \rho_i \sqrt{T} F_i^1 \right\} \quad i = 1, 2, \dots, n \quad (\text{III-9})$$

$$\rho \left[u^2 + \frac{RT}{M} \right] = R \sum_{i=1}^n \frac{1}{M_i} \left\{ \frac{1}{2} \alpha_i \rho_{s_i} T_s + (2-\alpha_i) \beta \rho_i T F_i^2 \right\} \quad (\text{III-10})$$

$$\rho u \left[\frac{5}{2} \frac{RT}{M} + \frac{1}{2} u^2 \right] = \sqrt{\frac{1}{2\pi}} (RT_s)^{3/2} \sum_{i=1}^n \left\{ \frac{\alpha_i}{2} \frac{\gamma_i+1}{\gamma_i-1} \frac{\rho_{s_i}}{M_i^{3/2}} \right\}$$

$$+ \frac{\beta(RT)^{3/2}}{\sqrt{2\pi}} \sum_{i=1}^n \frac{\alpha_i \rho_i F_i^3}{M_i^{3/2}}$$

$$- \frac{RT_s^{1/2} T}{\sqrt{2\pi}} \sum_{i=1}^n \left\{ \frac{\alpha_i}{2} G(\gamma_i) \frac{\rho_{s_i}}{M_i^{3/2}} \right\} \quad (\text{III-11})$$

where $G(\gamma_i) = (5 - 3\gamma_i)/2(\gamma_i - 1)$, subscript i designates the species i values of the quantity, and the F functions are given by

$$F_i^1 = \left[\pi^{1/2} m_i \operatorname{erfc}(m_i) - e^{-m_i^2} \right] \quad (\text{III-12a})$$

$$F_i^2 = \left[\left(m_i^2 + \frac{1}{2} \right) \operatorname{erfc}(m_i) - m_i \pi^{-1/2} e^{-m_i^2} \right] \quad (\text{III-12b})$$

$$F_i^3 = \left[m_i \left(m_i^2 + \frac{5}{2} \right) \pi^{1/2} \operatorname{erfc}(m_i) - \left(m_i^2 + 2 \right) e^{-m_i^2} \right] \quad (\text{III-12c})$$

$$m_i = \frac{u_i}{\sqrt{2RT}} \quad (\text{III-12d})$$

In order to solve these equations, additional information is required. A portion of this information is obtained from the chemistry of the system. Here we assume frozen chemistry, i.e., no chemical reactions at all take place between the different carbon species. Since no reactions occur, the ratio of the species i mass fraction K_i to the total mass fraction must be the same as the ratio of the mass flux of species i leaving the surface to the total mass flux. In other words,

$$\frac{K_i}{1} = \frac{\dot{m}_i}{\dot{m}} \quad (\text{III-13a})$$

Substituting $K_i = \rho_i/\rho$, $\dot{m}_i = \rho_i u_i$ and $\dot{m} = \rho u$, Eq. (III-13a) becomes

$$u_i = u \quad (i=1,2,\dots,n) \quad (\text{III-13b})$$

Additional equations required to close the system are

$$\rho = \sum_{i=1}^n \rho_i \quad (\text{III-14a})$$

$$\frac{1}{M} = \frac{1}{\rho} \sum_{i=1}^n \frac{\rho_i}{M_i} \quad (\text{III-14b})$$

$$p_i = \frac{\rho_i RT}{M_i} \quad (\text{III-14c})$$

$$p_e = \sum_{i=1}^n p_i \quad (\text{III-14d})$$

and the surface energy balance equation (III-7), where \dot{m} and h are now given by

$$\dot{m} = \rho u = \sum_{i=1}^n \rho_i u_i \quad (\text{III-14e})$$

$$h = \sum_{i=1}^n K_i h_i \quad (\text{III-14f})$$

For specified I_0 and p_e , Eqs. (III-9) through (III-14) may be solved simultaneously using an iterative procedure and guessing the temperature T_s as described in Subsection III-B. For the guessed temperature, the carbon species vapor pressure p_{s_i} for $i = 1, 2, \dots, n$ may be calculated from thermochemical data and subsequently used to determine the ρ_{s_i} .

2. Problem Formulation - Equilibrium Case

Equilibrium chemistry in the Knudsen layer represents the opposite bounding case to that of frozen chemistry, i.e., chemical reactions take place between all the carbon species at rates sufficient to ensure local chemical equilibrium. Thus, in the system of equations given by Eqs. (III-9) through (III-14), it is necessary to replace those equations limited to frozen chemistry by alternate equations applicable to equilibrium chemistry.

When chemical reactions take place, the n equations given by Eq. (III-13b) no longer are valid. However, if chemical equilibrium is achieved at the edge of the Knudsen layer, the species partial pressures p_i are given by

$$p_i = \left[\frac{p_1}{p_{s_1}(T)} \right]^i p_{s_i}(T) \quad i = 2, 3, \dots, n \quad (\text{III-15a})$$

where T is the temperature at the edge of the Knudsen layer. The n^{th} independent equation is

$$\rho u = \sum_{i=1}^n \rho_i u_i \quad (\text{III-15b})$$

3. Calculated Results and Applications

A basic objective of this work is to obtain carbon species thermochemical data information from laser heating experiments. For specified thermochemical data which define the carbon species vapor pressures p_{s_i} and assumed vaporization coefficients α_i , the equations described above allow the mass loss rate m and the surface temperature T_s to be calculated as a function of the ambient pressure p_e and the laser radiation heat flux I_0 . The results of calculations using a somewhat simplified set of Eqs. (III-9) through (III-11), assuming frozen chemistry in the Knudsen layer, JANNAF thermochemical data, and unit vaporization coefficients, are shown in Fig. 14.

Comparison of these predicted results with laser-heated carbon ablation data should allow one to determine the validity of the JANNAF data and the unit vaporization coefficient assumption. However, as discussed in our earlier work with linearized models^{4,5}, a uniqueness problem arises; i.e., the measured mass loss rate and surface temperature can be predicted using JANNAF thermochemical data (which give relatively low carbon total vapor pressure) with unit vaporization coefficients, as in Fig. 14, or by using other thermochemical data^{15,16}, which give carbon total vapor pressures up to an order of magnitude larger than the JANNAF data, with reduced values of the vaporization coefficients.

15

Kratsch, K.M., et al., "Graphite Ablation in High Pressure Environments," AIAA Paper 68-1153, 1968.

16

Dolton, T.A., H.E. Goldstein, and R.E. Mauer, "Thermodynamic Performance of Carbon in Hyperthermal Environments," Progress in Astronautics and Aero-nautics: Thermal Design Principles of Spacecraft and Entry Bodies, 21, J.T. Bevans (ed.), AIAA, New York, 1969, pp. 169-201.

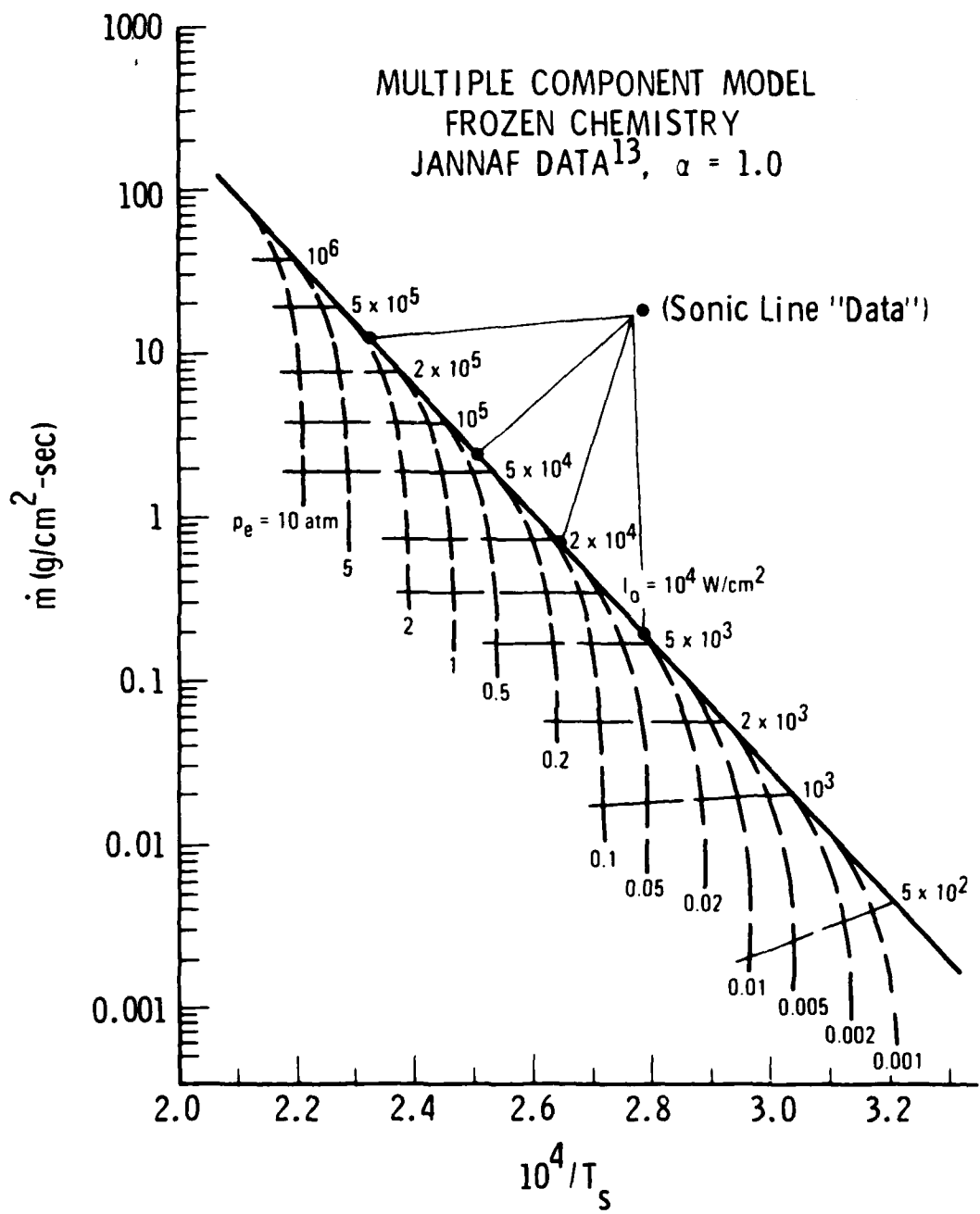


Fig. 14. Mass Loss Rate as a Function of Radiation Intensity and Ambient Pressure

In an attempt to resolve the uniqueness problem, sensitivity calculations were carried out to determine if experimental mass loss and surface temperature data could be taken in such a way as to uniquely determine the vapor pressure (and thus the thermochemical data) and the vaporization coefficients from the data. Mass loss rate \dot{m} and surface temperature T_s were treated as dependent variables to be measured. The main question is, How should the ambient pressure p_e and the laser radiation heat flux I_0 be varied in order to obtain unique information from the measured \dot{m} and T_s ?

An early conclusion, in line with previous work using the linearized nonequilibrium phase change model, was that if all the data are taken such that the outward flow at the surface is sonic (solid line on Fig. 14), then uniqueness cannot be established. For instance, suppose we had experimental data represented by the four *'s on Fig. 14. We see that the JANNAF thermochemical data with unit vaporization coefficients predict the "data." However, other thermochemical data which give higher total vapor pressure also predict the "data" using smaller vaporization coefficients.

To eliminate this impasse, sensitivity calculations were made for potential experimental data in the subsonic regime, i.e., the dashed lines region of Fig. 14. Two chemistries were used: JANNAF and Lee and Sanborn¹⁷. The Lee and Sanborn thermochemical data were selected to compare with JANNAF because they are more recent than others we have used previously^{13,15,16} and give carbon total vapor pressures only 2.5 to 3 times higher than JANNAF. In comparison, thermochemical data of Refs. 15 and 16 result in predicted carbon total vapor pressures an order of magnitude above JANNAF for temperatures greater than 4000°K. Thus, if a method of obtaining experimental data could be identified which would allow one to choose uniquely between JANNAF and Lee and Sanborn thermochemical property data, then the same method surely could be used to consider other thermochemical data which differ from JANNAF to a much greater degree than that of Lee and Sanborn.

¹⁷

Lee, E.L. and R.H. Sanborn, "Extended and Improved Thermal Functions for the Gaseous Carbon Species C₁-C₇ from 298 to 1000 K," High Temperature Science, 5 1973, pp. 438-453.

It was found that for an assumed carbon species C_1 vaporization coefficient α_1 of 0.73, and also assuming $\alpha_i = (\alpha_1)^i$, $i = 2, 3, \dots n^{18}$, the predicted results using Lee and Sanborn chemistry matched those calculated using JANNAF chemistry with $\alpha_1 = 1.0$, and both calculations matched the sonic line "data" represented by the four •'s on Fig. 14.

It was assumed for the calculated results shown in Fig. 15 that experimental data could be taken in such a manner that I_0 and p_e varied so as to keep the surface temperature constant. The four •'s on Fig. 15 correspond to those on Fig. 14. For each of the four constant values of surface temperature, the external pressure p_e was increased and the laser radiation heat flux I_0 was decreased so as to keep T_s constant. The calculated results show very significant differences in behavior between the JANNAF chemistry and Lee and Sanborn chemistry predictions. Even though both chemistries match the hypothetical sonic flow data represented by the •'s, the external pressure increase to cause an order of magnitude decrease in \dot{m} is about a factor of four above the sonic pressure value p_e^* , if the JANNAF thermochemical data are correct, whereas a factor of eight-nine increase is required if the Lee and Sanborn chemistry is correct. This is excellent sensitivity, but data are required at constant temperature which is difficult to obtain.

It is much easier to obtain data at constant ambient pressure. Similar calculations for these two chemistries varying the laser heat flux I_0 but keeping ambient pressure constant are shown in Fig. 16. Along the sonic line, both chemistries match the four "data" points with different vaporization coefficients as before. However, if additional data could be obtained at constant pressure, it should be possible to select JANNAF or Lee and Sanborn chemistry, especially for $p_e = 1$ atm where the predicted surface temperatures T_s for the nearly vertical portions of the curve differ by 140^0K for the two chemistries.

18

Rosenblatt, G., Personal Communication, Department of Chemistry, Pennsylvania State University, University Park, Pa., Dec. 1979.

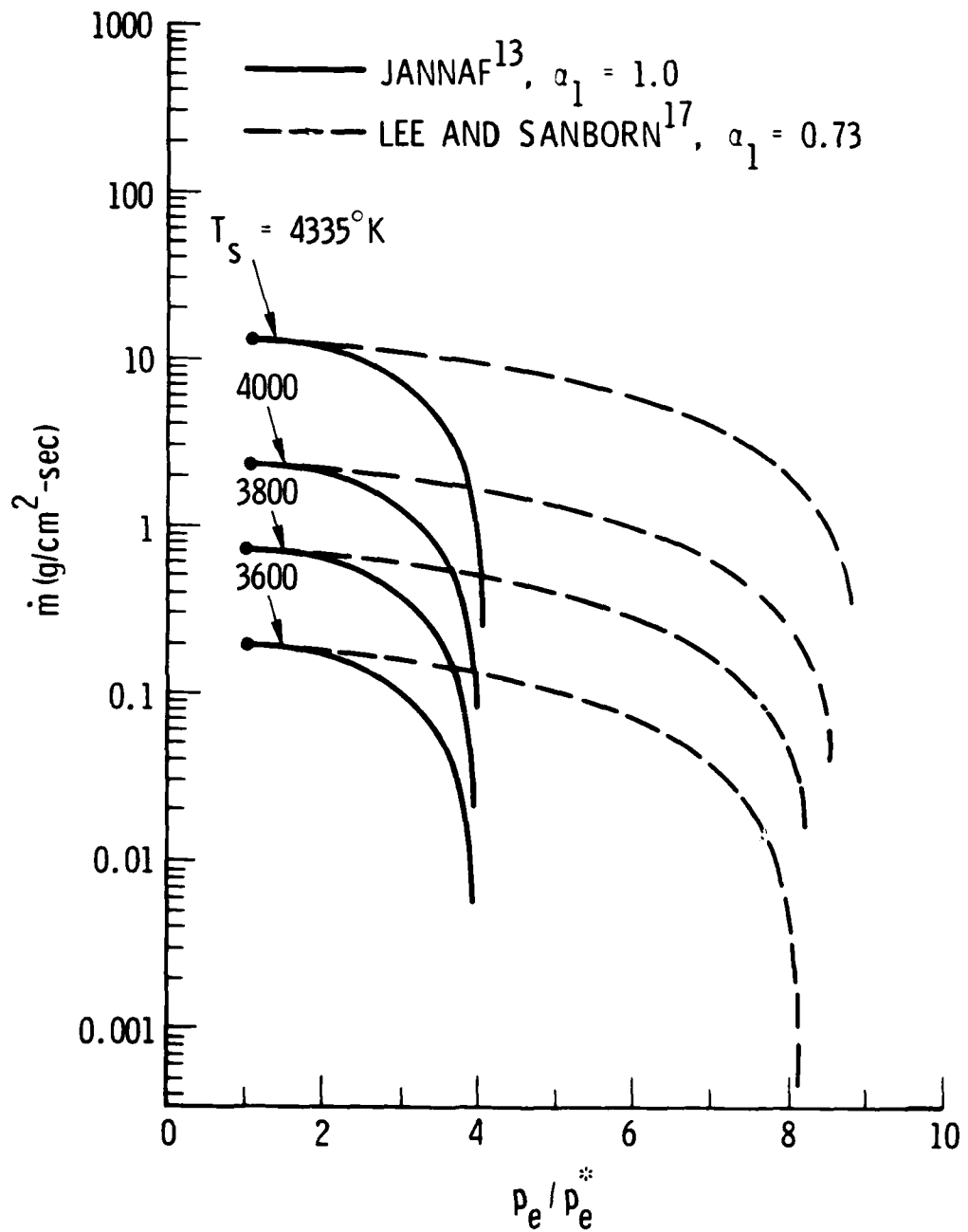


Fig. 15. Mass Loss Rate Behavior at Constant Solid Temperature T_s

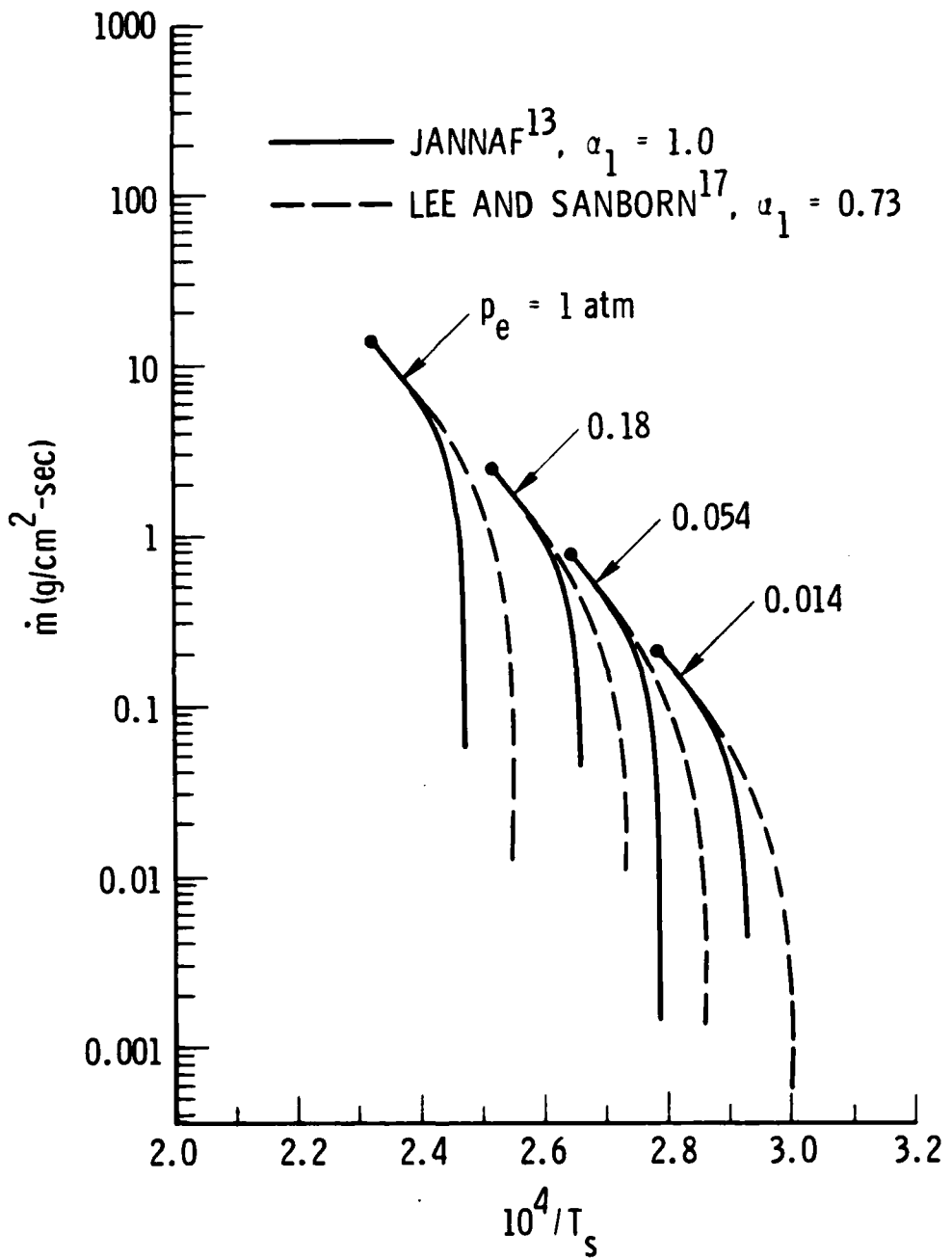


Fig. 16. Mass Loss Rate Behavior at Constant Ambient Pressure p_e

The above discussion leads to a conclusion which is very important but has not been previously recognized. It is illustrated in Fig. 17. Whereas in Fig. 16 two chemistries were considered with different vaporization coefficients for each, in Fig. 17 JANNAF frozen chemistry predicted results are shown for a range of vaporization coefficient α_1 values. It is obvious from this figure that the nearly vertical rapid rise in \dot{m} with T_s is independent of vaporization coefficient. Furthermore, it depends only on the vapor pressure and the ambient pressure which, for the vertical portion of the curve, are to a very good approximation equal to one another. Thus, we conclude from Figs. 16 and 17 that a rapid rise in the \dot{m} versus $1/T_s$ curve, from experimental data at constant ambient pressure p_e , can be used to uniquely determine vapor pressure at the experimentally measured value of T_s . The same data as well as other data along the sonic line could then be used to determine vaporization coefficients from measured mass loss rate, \dot{m} , values.

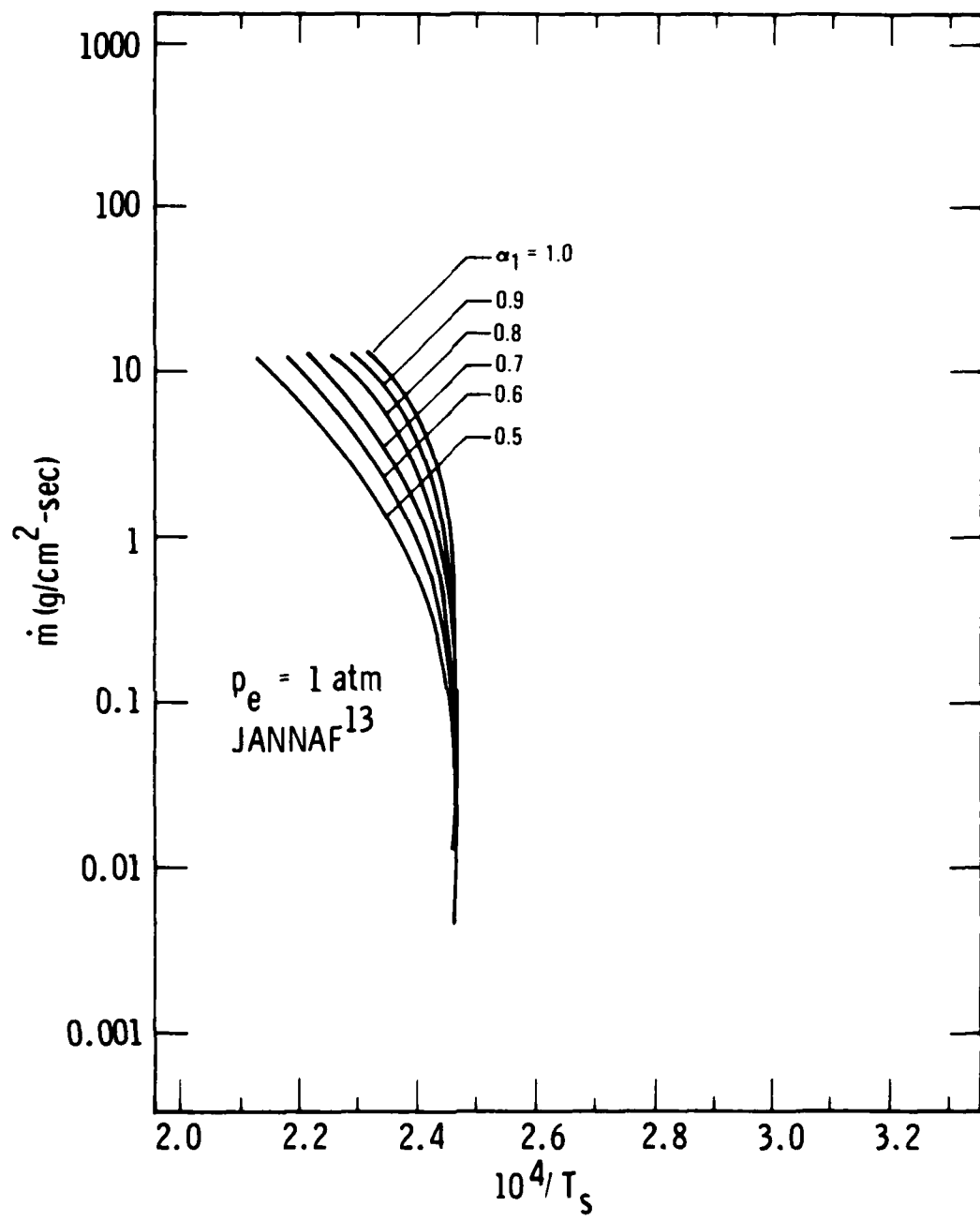


Fig. 17. Effect of Vaporization Coefficient on Predicted Mass Loss Rates

IV. CONTINUOUS WAVE LASER DATA

A. MATERIALS, EXPERIMENTAL FACILITY, TEST APPARATUS, AND INSTRUMENTATION

1. Materials

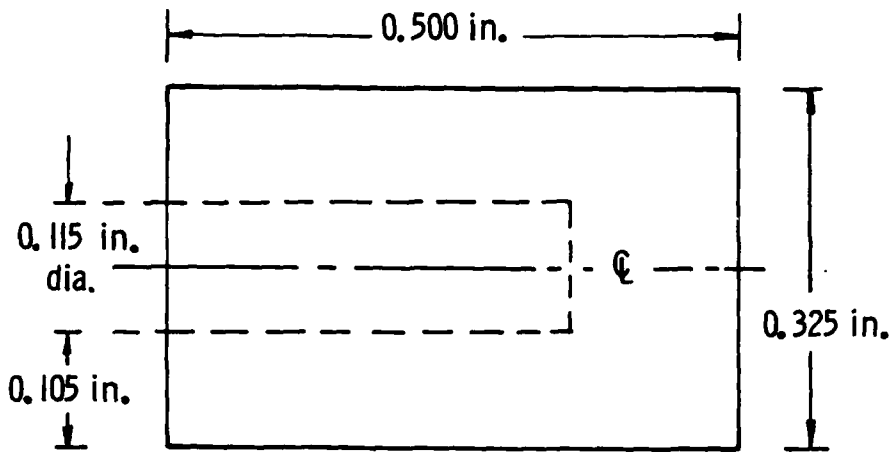
Two types of carbon were used in both the continuous wave (CW) laser tests reported here and the pulsed laser tests discussed in Section V. For both carbon types, samples from the same lot numbers were used in the CW and pulsed testing to ensure meaningful data comparisons. The two carbon types tested were pyrolytic graphite (PG) (Super Temp Company, continuously nucleated) and Graphnol (produced by Great Lakes Carbon Research Corporation for the Naval Surface Weapons Center). Cylindrical samples of both types of carbon with dimensions as shown in Fig. 18 were fabricated. The hole in one end of the sample facilitated spinning the sample by mounting it on a mandrel which could be rotated about its axis at up to 40,000 rpm. For the PG, the cylindrical surface was a-face and the flat ends were c-face. Slotted Graphnol samples were prepared when it became apparent from initial test data on the nonslotted Graphnol samples that significant convective and radiative heat loss was occurring due to conduction toward the mandrel-support end of the sample.

2. Experimental Facility

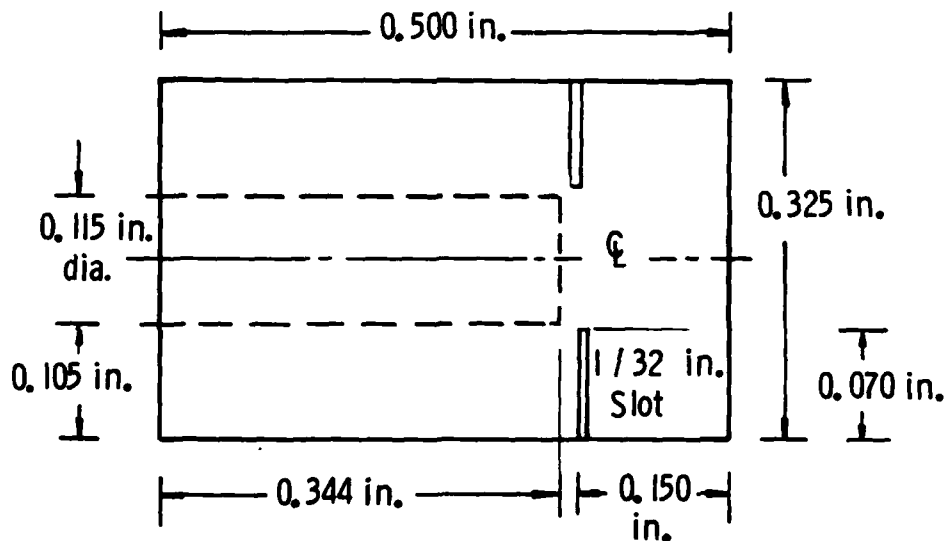
The experiments were carried out using the CO₂ electric discharge laser located at the Philco-Ford facility at Newport Beach, California. This laser had been used previously on four other occasions to carry out similar testing. A summary of the results of these tests recently has been prepared by Whittaker, et al.¹⁹. The maximum output power in the current tests was

¹⁹

Whittaker, A.G., et al., "Carbon Vapor Pressure in the Range 3450-4500 K and Evidence for Melting at ~3800 K," to be submitted to High Temperature Science.



(a) Pyrolytic Graphite and Graphnol Samples



(b) Slotted Sample, Graphnol Only

Fig. 18. Sample Geometry

6.4 kW. The $10.6 \mu\text{m}$ beam was approximately 8 cm in diameter with a flat (top hat) power distribution across the beam. Run times varied from 2 to 12 sec, depending upon the power density on target as related to sample survival time and the specific objectives of the run. Beam power was measured by reflecting part of the beam to a calorimeter. For a given laser power, power density on the target could be varied over a significant range by using a variable aperture²⁰ centered in the beam in front of the calorimeter. Estimated time to full laser power was 1 to 1.5 sec from test initiation. To compensate for this, a quick-acting reflective shutter was available and utilized in a portion of the tests. By delaying the shutter to open nominally 2 sec after test initiation, full laser power on the sample from the initial exposure could be assured.

3. Test Apparatus and Instrumentation

A schematic diagram of the test apparatus is shown in Fig. 19. The pressurizable test chamber was made of brass tubing about 50 cm long with an inside diameter of just over 50 cm. The end plate, viewing window, and smaller NaCl laser windows were sealed with O-ring seals. The focusing lens reduced the beam diameter from the nominal 8 cm output diameter received from the laser to a 3.5 mm spot diameter on the rotating cylindrical carbon sample.

The test chamber could be pressurized from 0.1 to 800 torr with Ar, O₂, or arbitrary mixtures of these gases. For tests conducted at one torr, the chamber was operated in an open configuration with a continuous flow of the pressurizing gas into and out of the chamber. For higher chamber pressures, a closed configuration was used. Pressures up to 10.0 torr were measured using a Baratron gage, while pressures in the 10 to 800 torr range were determined using a 25.4 cm Heise gage.

²⁰

Whittaker, A.G., et al., "System Employing Laser Heating for the Measurement of High-temperature Properties of Materials over a Wide Pressure Range," Review of Scientific Instruments, 48(6), June 1972, pp. 632-639.

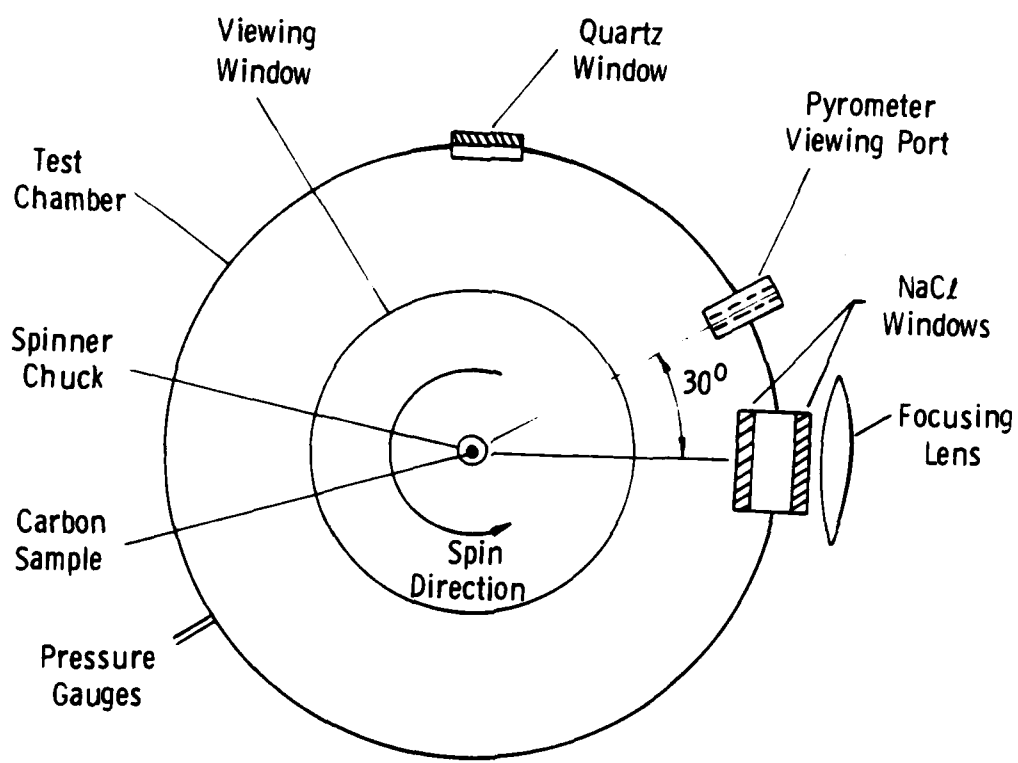


Fig. 19. Test Apparatus

Surface temperatures of the carbon samples were measured by an Ircon optical pyrometer which viewed the rotating sample 30 deg away from the laser beam axis in the direction of sample rotation. The area viewed by the pyrometer was a circular spot approximately 1 mm in diameter. Spectroscopic data were obtained from the carbon gas plume by means of the quartz viewing window at the top of the chamber. The spectrograph was focused at a point 2.5 mm from the sample surface on the axis of the laser beam. For selected runs, a high-speed (Hycam) camera was used to obtain motion pictures (7000 frames per second) through the front viewing window, and particles from the rotating sample were caught in a tray placed in the chamber.

An eight-channel Visicorder was used to record data during each test run. Signals from the laser power calorimeter, pyrometer, Baratron pressure gage, spectrograph shutter, and the time-delay reflective shutter were recorded in time sequence. A more detailed description of a similar, but smaller, test chamber with the same instrumentation is given by Whittaker, et al.²⁰.

B. TEST PLANNING

Final planning for this test series was carried out after the multiple component, nonlinear Knudsen layer model described in Section III had been developed utilizing, in particular, results of the sensitivity analyses. As discussed in Subsection III-C, experimental data obtained under conditions (laser power and ambient pressure) for which the flow in the laser-induced plume away from the ablating surface is subsonic are particularly useful. This is because appropriate data of this type can be used to uniquely determine vapor pressure and vaporization coefficients.

Consequently, the test matrix for these experiments was planned using the following guidelines:

1. Obtain almost all data in the subsonic plume region.
2. Locate experimentally the nearly vertical portions of the m versus $1/T_s$ (see Fig. 14) curves by conducting tests at constant ambient pressure for a series of laser power levels.

3. Locate the limiting sonic line in the \dot{m} versus $1/T_s$ plane by
 - a. Conducting tests at several moderate to high laser power levels for an ambient pressure of one torr (thus assuring sonic flow at the Knudsen layer edge).
 - b. Conducting tests at constant laser power and reducing the chamber pressure incrementally until doing so no longer reduces the surface temperature, i.e., the flow has choked and is therefore sonic at the Knudsen layer edge.
4. Obtain mass loss rate \dot{m} for all tests by weighing before and after the tests.
5. Select run conditions for constant ambient pressure tests (2, above) and constant laser power tests (3, above) in such a way as to obtain, as nearly as possible, experimental data at constant surface temperature.

C. DATA SUMMARY

In line with the above guidelines, the test matrices as carried out are summarized in data Tables 1 and 2 for Graphnol and PG, respectively. Since laser power and ambient chamber pressure are the independent variables in these experiments, individual values of these parameters for each data run are given in the column at the left and the row at the top, respectively, of each table. Within the box corresponding to the intersection of a given laser power and ambient pressure, the sample number, length of the run, measured surface temperature, and mass loss rate are given.

Potentially useful data were obtained on a total of about 85 samples at laser power levels ranging from 1.0 to 6.4 kW and at ambient chamber pressures of 0.5 to 800 torr. Except as noted in the tables, for all pressure levels above one torr the chamber gas was an equal molar mixture of Ar and O₂. All tests at one torr or below were pure O₂. As discussed in Ref. 19, the oxygen was necessary in order to eliminate voluminous soot formation which can completely obscure the pyrometer data and significantly reduce the power transmitted to the sample by coating the laser window and absorbing laser energy within the carbon vapor plume.

Table 1. Graphol Data

P _e , torr	1	38	76	152	380	760	800
Laser Power							
1.01 kW	9, 12 sec ----- 0.4 mg/sec						
1.45 kW	10, 12 sec 28700K 0.4 mg/sec						
1.96 kW	11, 11 sec 33350K 0.8 mg/sec						
2.04 kW	21, 7 sec 32170K 0.7 mg/sec						
2.10 kW			35, 7 sec 34000K 5.81 mg/sec				
2.33 kW	7, 10 sec 34660K 2.63 mg/sec						
2.41 kW					91C, 8 sec 35210K 4.66 mg/sec		
2.76 kW			56, 7 sec 35320K 7.73 mg/sec				
2.83 kW	5, 8 sec 35350K 6.45 mg/sec						
2.83 kW	6, 10 sec 35300K 4.63 mg/sec						
2.91 kW	3, 6 sec 35320K 2.50 mg/sec						
2.98 kW	4, 10 sec 35650K 6.5 mg/sec						
2.98 kW	79, 8 sec 35260K 4.9 mg/sec						
3.05 kW	2, 8 sec 35650K 6.2 mg/sec						
3.05 kW	12, 7 sec 35200K 4.5 mg/sec						
3.05 kW		83, 6 sec 35700K 9.15 mg/sec					

Table 1. Graphnol Data (Continued)

P_e , torr	1	38	76	152	380	760	800
Laser Power							
2.90 kW			81, 8 sec 35650K 4.64 mg/sec				
2.98 kW					90C, 7 sec 36870K 17.1 mg/sec		
3.05 kW					54, 8 sec 36480K 15.4 mg/sec		
2.98 kW	5% O ₂ 95% Ar				84, 8 sec 34830K 1.71 mg/sec		
2.91 kW	10% O ₂ 90% Ar				85, 8 sec 35160K 2.49 mg/sec		
3.41 kW	23% O ₂ 77% Ar				47, 8 sec 36540K 6.32 mg/sec		
3.19 kW					89C, 6 sec 36810K 16.9 mg/sec		
3.34 kW		82, 6 sec 36090K 14.9 mg/sec					
3.41 kW			57, 7 sec 36310K 15.2 mg/sec				
3.63 kW					48C, 5 sec 37540K 18.4 mg/sec		
3.99 kW					49C, 5 sec 37770K 23.2 mg/sec		
4.07 kW	22, 5 sec 36000K						
4.21 kW					69C, 5 sec 37940K 29.6 mg/sec		
4.29 kW	8, 7 sec 35870K 18.2 mg/sec						
4.36 kW	1, 8 sec 36870K 17.7 mg/sec						

Table 1. Graphnol Data (Concluded)

P_e , torr	1	38	76	152	380	760	800
Laser Power							
4.36 kW			45C, 5 sec 36650K 16.7 mg/sec				
4.36 kW			50, 5 sec 36420K 17.7 mg/sec				
4.36 kW				46C, 5 sec 36870K 23.7 mg/sec			
4.36 kW					70C, 5 sec 38330K 30.9 mg/sec		
4.50 kW					92C, 5 sec 37430K 40.7 mg/sec		
4.58 kW						52, 6 sec 38300K 28.4 mg/sec	
4.58 kW						53, 7 sec 38330K 28.7 mg/sec	
4.87 kW		51, 4 sec(S) 36310K 30.1 mg/sec					
4.94 kW						100C, 4.5 sec(S) 38330K 79.6 mg/sec	
5.08 kW						99, 4.5 sec(S) 38110K 69.0 mg/sec	
5.28 kW				47C, 5 sec ----- 34.6 mg/sec			
5.30 kW			32, 7 sec 36420K -----				946, 4 sec 38840K 59.0 mg/sec
5.37 kW	48, 4 sec(S) 35820K 55.5 mg/sec					95, 4 sec(S) 38670K 110 mg/sec	
5.81 kW							
6.39 kW					96, 4 sec(S) 38330K 90.7 mg/sec		

Table 2. Pyrolytic Graphite Data

p_e , torr	0.5	1	3.8	15.2	38	76	152	190	380	380	760
Laser Power											
1.59 kW				17.7 sec 3384°K 0.8 mg/sec							
1.89 kW				16.12 sec 3459°K 1.6 mg/sec							
2.18 kW											
2.32 kW											
2.47 kW				18.7 sec 3560°K 2.9 mg/sec							
2.83 kW				15.4 sec 3592°K 4.0 mg/sec							
2.90 kW											
2.90 kW											
3.05 kW				60.6 sec 3587°K 4.4 mg/sec							
3.2 kW				14.6 sec 3612°K 7.6 mg/sec							
3.34 kW											
3.34 kW											
					59.6 sec 3681°K 6.6 mg/sec	44.6 sec 3697°K 9.8 mg/sec	43.6 sec 3699°K 8.2 mg/sec	40.6 sec 3640°K 14.2 mg/sec	39.6 sec 3690°K 16.0 mg/sec	38.6 sec 3830°K 19.1 mg/sec	37.6 sec 3880°K 17.3 mg/sec

Table 2. Pyrolytic Graphite Data (Continued)

P_0 , torr	0.5	1	3.8	15.2	38	76	152	190	380	760
Laser Power										
3.34 kW										
3.79 kW										
3.85 kW	13.6 sec 3700K									
3.92 kW										
4.10 kW										
4.58 kW										
4.72 kW										
4.87 kW										
5.29 kW										
6.39 kW										
6.39 kW										

An equal molar mixture of Ar and O₂ was selected because this percentage of O₂ was the minimum amount required for ambient pressures near 76 torr, and it was felt that maintaining a constant mixture ratio for all total pressures was desirable. At ambient pressures significantly below 76 torr, O₂ mole fractions greater than 50 percent are required. Thus, data at one torr were obtained using 100 percent O₂.

D. PRELIMINARY DATA ASSESSMENT

The tests were conducted in the tenth month of the contract year. The time since then has been devoted mainly to reducing the data to obtain mass loss, mass loss rate, and sample surface temperatures for each run. This information is summarized in Tables 1 and 2 for the Graphnol and PG samples, respectively. In terms of the guidelines discussed in Subsection IV-B, the scope of the data obtained is considered to be very good. In the following, the post-test appearance of selected samples of both types of carbon are first discussed in order to put planned detailed data analysis in the proper perspective. Then, a preliminary data analysis is presented, comparing predicted results with experimental data with the objective of obtaining carbon vapor pressure and vaporization coefficient information.

1. Post-Test Appearance - Graphnol Samples

The cylindrical carbon samples with pretest geometries as shown in Fig. 18 were irradiated with the 3.5 mm diameter laser beam focused toward the end of the sample, where the carbon material being tested extended all the way to the cylinder axis. This was done in order to maximize the amount of material available to be ablated away, as well as to minimize the energy lost by heat conduction into the spinner mandrel. Most samples were spun at a rate of 20,000 rpm.

For the Graphnol samples, this resulted in a relatively symmetric groove of various depths, depending upon the laser power. An example of such a groove for a low pressure (one torr) run of 8-sec duration with a peak laser power of 4.35 kW is shown in Fig. 20. The surface of the ablated carbon in the groove is relatively smooth as a result of the fine grain structure of the Graphnol sample. Outside the groove on the cylinder surface, a wide band of vapor-deposited carbon with a grey surface appearance is seen. This material may be one of the carbynes²¹ recently discussed by Whittaker²². The black material visible on top of the sample is soot.

Further examples of the post-test appearance of Graphnol samples are shown in Fig. 21. Each of the three samples was exposed to a nominal laser power of 3 kW. The ambient pressures left to right were 380 torr, 38 torr, and one torr. The width of the vapor-deposited grey band decreases significantly at the higher ambient pressures. This is because the lateral expansion of the laser-induced plume of carbon vapor is greatly reduced as the ambient pressure is increased. Of greatest significance are the measured mass losses as given on the figure. Since the nominal laser power and, therefore, the power density on the samples was the same for all three samples, all of our previous linearized models as well as the multiple species nonlinear model of Subsection III-C would predict the mass loss rate for the three samples to be about the same. The very large increase in mass loss rate is due to the presence of O₂ in the chamber atmosphere. Thus, in the detailed data analysis, which will be proposed as a part of next year's contract, mass loss rates for Graphnol samples will need to be corrected for mass loss due to oxidation of solid carbon^{3,23} before vaporization coefficient information can be obtained. Most of the mass loss by oxidation is believed to occur from

²¹

Whittaker, A.G., Personal Communication, The Aerospace Corporation, El Segundo, Calif.

²²

Whittaker, A.G., "Carbon: A New View of Its High-Temperature Behavior," *Science*, 20, 19 May 1978, pp. 763-764.

²³

Doak, R.B. and J.R. Baron, "Activation Studies in Graphite Oxidation," Progress in Astronautics and Aeronautics: Rarefied Gas Dynamics, 51(II), J.L. Potter (ed.), AIAA, New York, 1977, pp. 621-634.

Ambient Pressure: 1 torr
Laser Power: 4.36 kW
Duration: 12 sec (Sample 1)



Fig. 20. Graphnol Sample, Long Duration, Low Ambient Pressure Run

Ambient Pressure:	380 torr	38 torr	1 torr
Laser Power:	3.05 kW	3.05 kW	2.98 kW
Duration:	8 sec (Sample 54)	6 sec (Sample 83)	8 sec (Sample 79)
Mass Loss Rate:	13.4 mg/sec	9.15 mg/sec	4.9 mg/sec

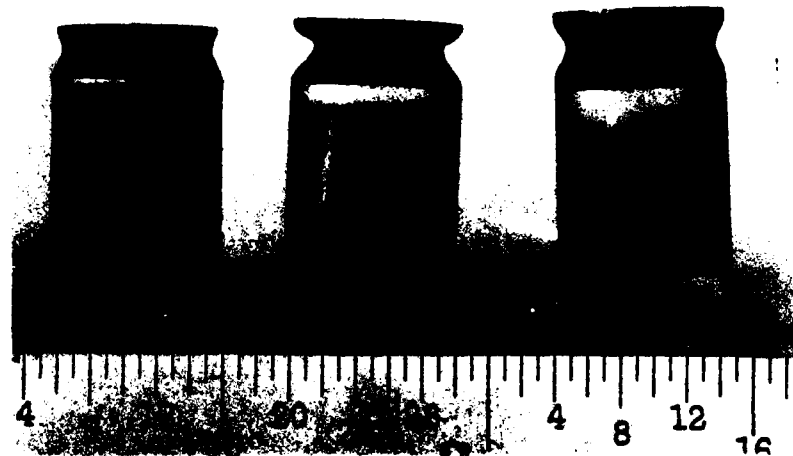


Fig. 21. Effect of Ambient Pressure at Constant Laser Power, Graphol Samples

the cylindrical surface away from the laser groove. For Graphnol, this entire surface becomes glowing hot during each run.

Other factors which somewhat complicate the accurate determination of mass loss rates for the Graphnol samples, but at the same time supply potentially very useful new information concerning the high temperature behavior of carbon, are shown in Figs. 22 and 23. The sample shown in Fig. 22 was exposed to a high power density for a short time with full power on the sample from its initial exposure through use of the time-delayed reflective shutter. The ambient pressure was relatively low. This resulted in the unique formation of the vapor-deposited globules barely visible on top of the sample in the left picture and shown in plan view on the right. In the past, similar globules have been interpreted at times as evidence of liquid carbon. This is highly unlikely in this case, as the maximum temperature reached by the sample was only 3582°K . It is speculated that the globules may be dendrites²¹. On the cylindrical surface, a thin vapor-deposited band of the previously described grey material can be seen along with a much wider band of soot.

The five samples in the pictures of Fig. 22 show the post-test appearance of slotted Graphnol samples. From Table 1, it is apparent that the slot did somewhat reduce energy loss due to conduction in that, for identical laser power and ambient pressure, a slotted Graphnol sample is likely to be 20 to 30°K higher in surface temperature. However, the slot also resulted in vapor deposition on the relatively cold surface formed by the slot and the main portion of the cylinder. In the upper picture, the carbon vapor-deposited ring is shown detached from the surface on which it formed due to differential expansion on cooldown. The sample on the right did not form a ring, possibly because of the relatively low ambient pressure. The three samples in the lower picture each have detached vapor-deposited rings as well as other possibly vapor-deposited material on the outside lip of the ablative mass loss groove.

Ambient Pressure: 38 torr
Laser Power: 5.37 kW
Duration: Total 4 sec, on sample ~2 sec (Sample 98)

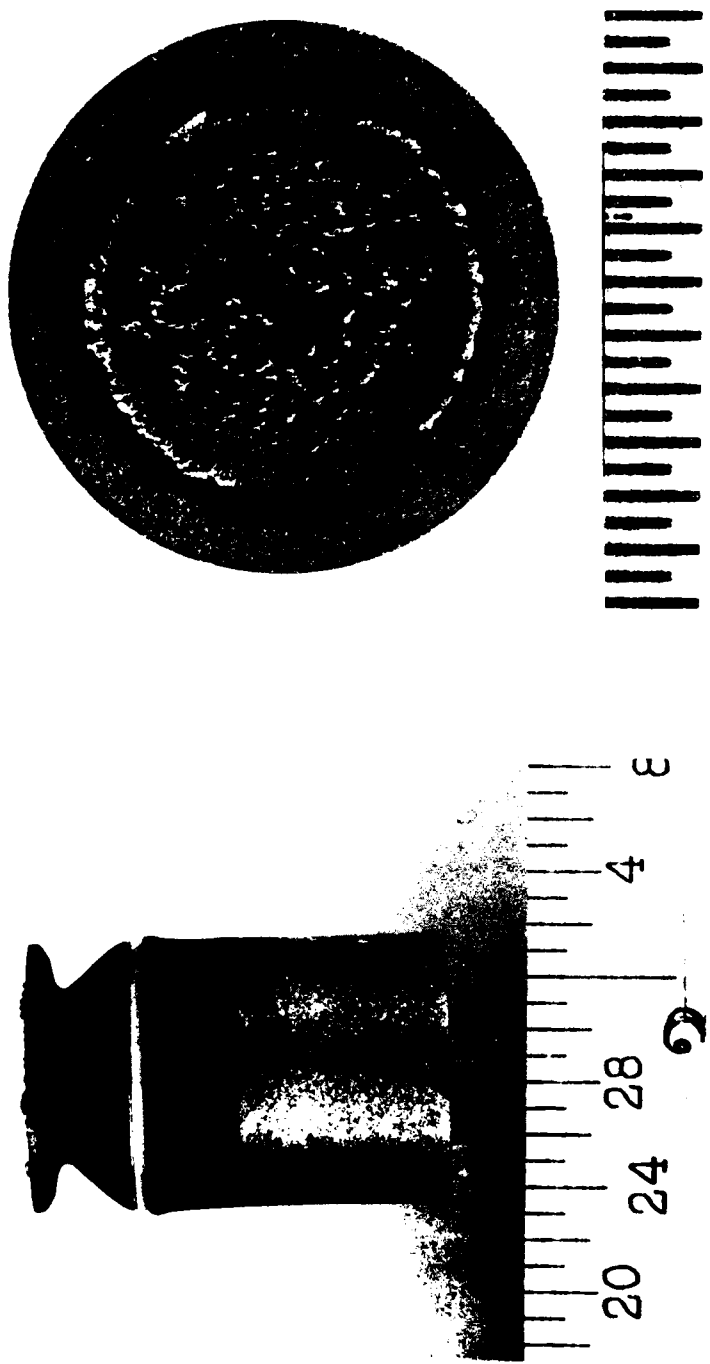


Fig. 22. Graphol Sample with Vapor-Deposited Globules

380 torr
5.23 kW
5 sec (Sample 47)



152 torr
4.36 kW
5 sec (Sample 46)

380 torr
3.05 kW
8 sec (Sample 88)



800 torr
5.1 kW
~3.5 sec (Sample 93)

Ambient Pressure: 380 torr
Laser Power: 4.5 kW
Duration: 5 sec (Sample 92)

Fig. 23. Slotted Graphnol Samples

2. Post-Test Appearance - Pyrolytic Graphite Samples

In contrast to the Graphnol samples, the ablation groove for the PG samples always showed an irregular profile. Examples of this are shown in Fig. 24. The two samples each saw about the same nominal laser power, the difference between the two being a fairly substantial difference in ambient pressure. The low pressure (152 torr) sample on the left shows an irregular groove and a silver-grey deposit on the cylinder surface outside the groove which extends down into the groove. The high pressure (760 torr) sample on the right has an irregular groove and a distinctly different surface appearance. The mass loss rates measured for these two samples are within 10 to 15 percent of each other, as would be expected, and in contrast to the Graphnol samples shown in Fig. 21 and discussed previously.

Thus, even though the material does not respond uniformly, with gouges appearing between graphite planes, the very low thermal conductivity perpendicular to the c-faces, i.e., in the direction parallel to the cylinder axis, localizes the heating to a fairly narrow strip not too much wider than the diameter of the laser beam. This prevents significant mass loss by oxidation of solid carbon on the cylindrical surface, as occurs for the Graphnol samples. This view is substantiated by the immediate post-test appearance of the samples just seconds after the laser has shut down. The PG samples at that time are glowing hot only in a band centered on the deepest part of the laser-produced groove in the sample. In contrast to this, the Graphnol samples at that time are glowing hot over the whole cylindrical surface.

PG samples exposed to a higher laser power and different pressures are shown in Fig. 25. In this case, the sample on the left showed significantly less mass loss (at the same laser power) due to voluminous soot formation which blackened the laser window and reduced the laser power density on the sample. A fairly thick and wide band of vapor-deposited soot can be seen on the cylindrical surface below the silver-grey band. The groove on this sample is highly irregular.

Ambient Pressure: 152 torr
Laser Power: 4.14 kW
Duration: 4 sec (Sample 71)
Mass Loss Rate: 28.3 mg/sec

760 torr
3.92 kW
4 sec (Sample 72)
25.2 mg/sec

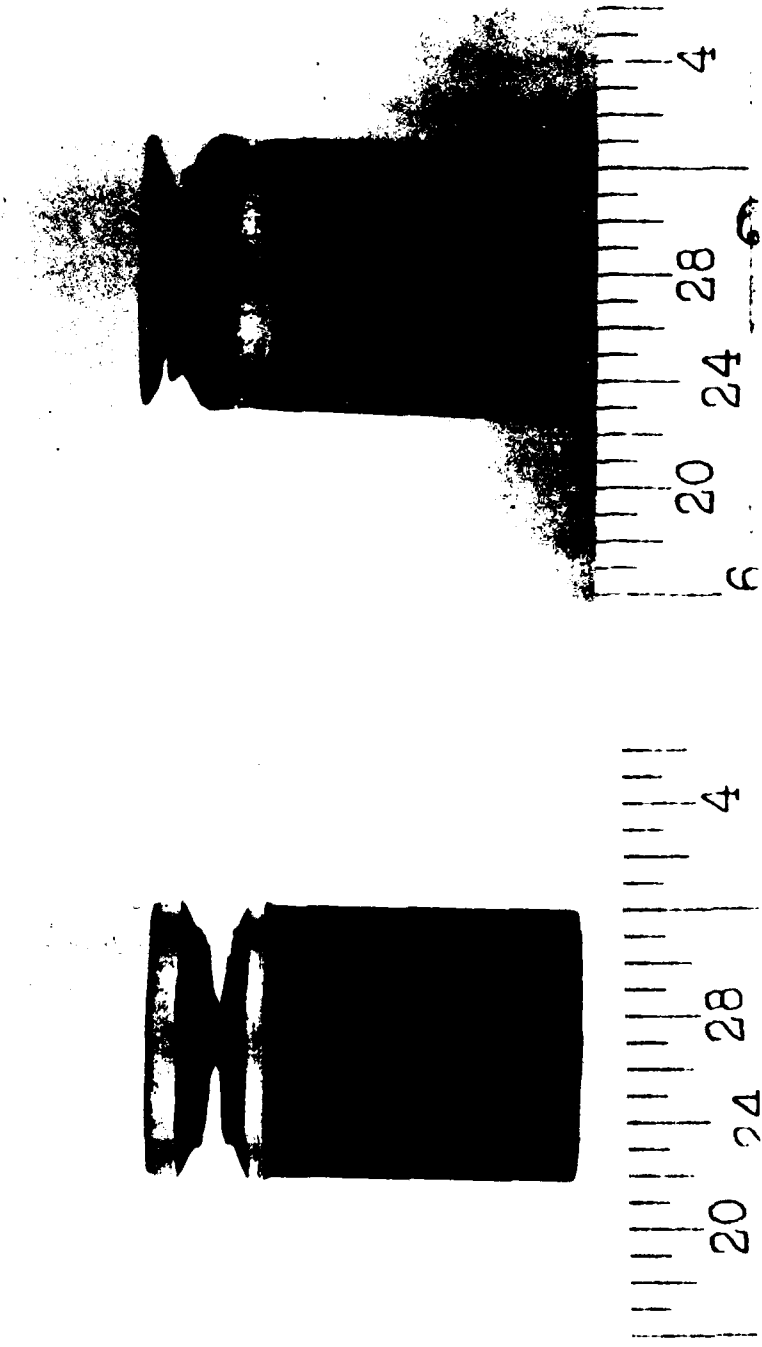


Fig. 24. Pyrolytic Graphite Samples, Effect of Ambient Pressure at Constant Laser Power

Ambient Pressure: 38 torr
Laser Power: 4.87 kW
Duration: 4 sec: ~2 sec on sample
(Sample 78)
Mass Loss Rate: 43 mg/sec

380 torr
4.72 kW
4.5 sec, ~2.5 sec on sample
(Sample 74)
65 mg/sec

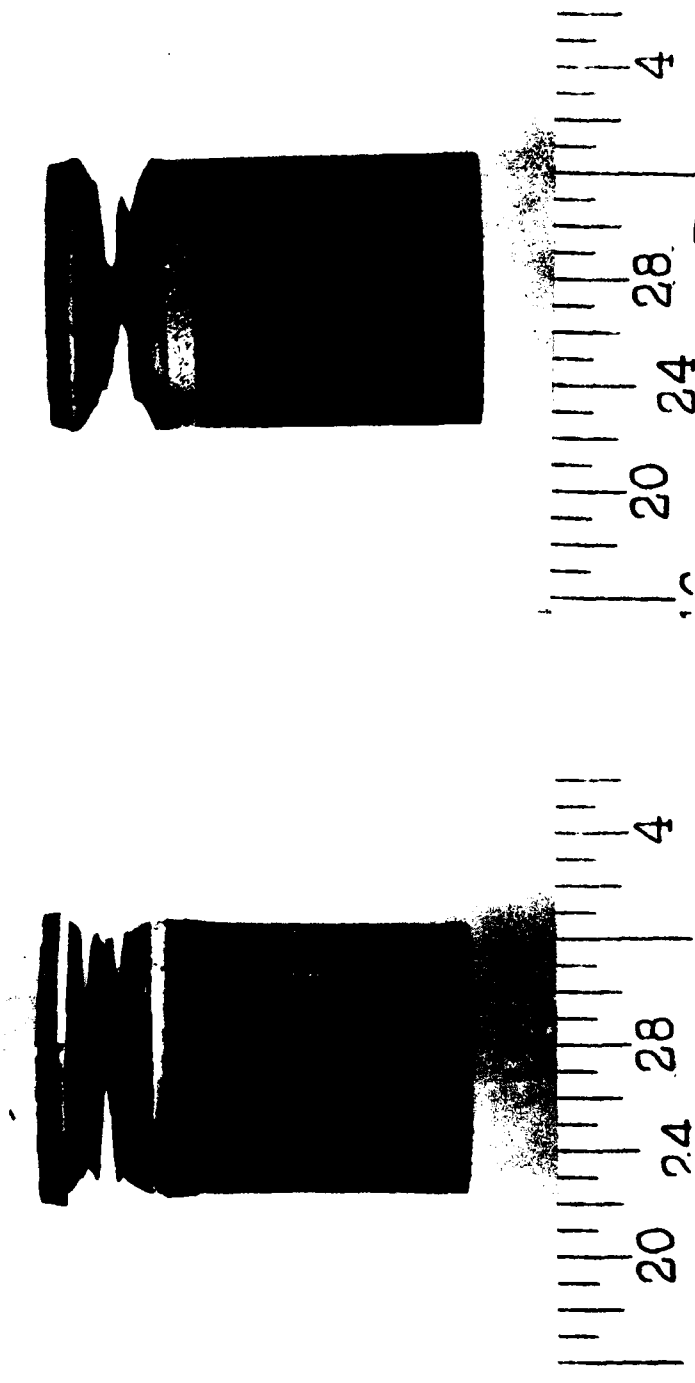


Fig. 25. Pyrolytic Graphite Samples, Effect of Ambient Pressure at Constant Laser Power, Showing Soot Deposition

3. Preliminary Data Analysis

To obtain carbon vapor pressure and vaporization coefficient information from the experimental data, the variation of the measured mass loss rates and surface temperatures is to be compared with theoretical predictions as discussed in Subsection III-C. A preliminary comparison of this type is shown in Fig. 26. The mass loss rates plotted in this figure are those tabulated in Tables 1 and 2. They were obtained simply by dividing the total measured mass loss by the total sample exposure time. Thus, no corrections for transients near time zero, mass loss by oxidation, or material vaporized and subsequently redeposited from the vapor have been made. However, the overall slope of the data in general follows the slope of the reference JANNAF line drawn for comparison.

Graphol data are given by the circles and PG data by the triangles. Filled symbols designate run conditions believed to correspond to sonic flow at the Knudsen layer edge, while open symbols designate run conditions predicted to give subsonic flow. The PG data tend to lie below the data for the Graphol, most likely due to significant mass loss by oxidation in the latter case. To obtain vapor pressure and vaporization coefficient information from these data, corrections for oxidative mass loss, transient heating, and vapor deposition, as well as correlation with the macroscopic energy balance to relate the data points to the laser power, will be required. We plan to proceed with the work necessary to accomplish these requirements.

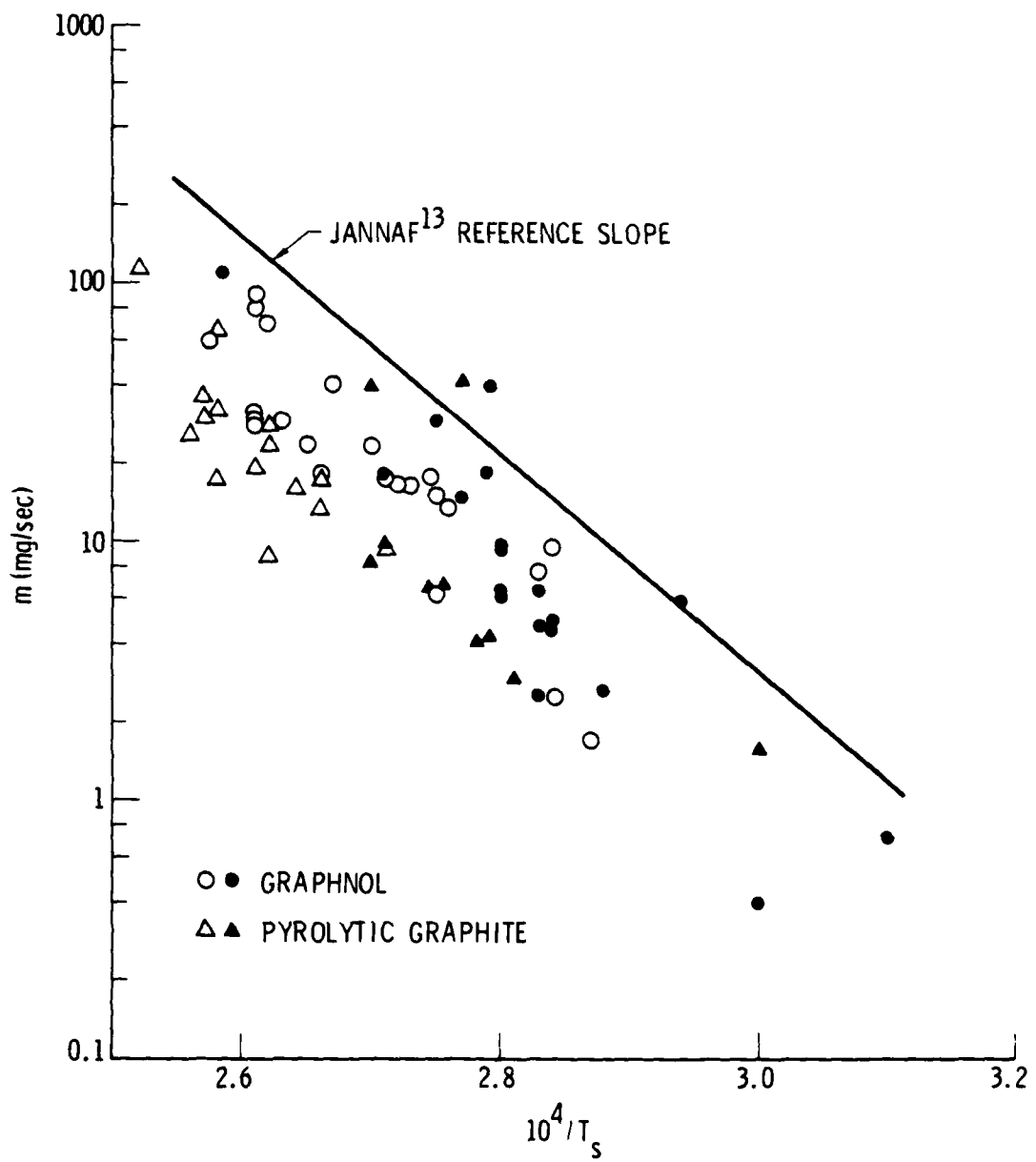


Fig. 26. CW Laser Ablation Data

79 / 80

V. PULSED LASER DATA

The two carbon types tested in these experiments were the same as those described in Subsection IV-A, pertaining to the CW laser tests. For each carbon type, samples from the same lot numbers were used in the CW and pulsed laser testing. Whereas the power densities on the carbon samples were 10 to 50 kW/cm² for the CW laser 10.6 μm radiation, the power densities in the pulsed tests discussed here were 200 kW/cm² up to 4 MW/cm² for the 1.06 μm neodymium-glass laser radiation. The corresponding maximum exposure times were about 10 sec and 1 msec, respectively. The data discussed here were obtained during the past year as part of a cooperative effort with the NASA Ames Research Center and have been documented recently by Covington²⁴.

A. CARBON VAPORIZATION EXPERIMENTS

1. Background

The laser, experimental technique, and apparatus used in these experiments²⁴ are described by Covington, et al.²⁵. The method utilized by Covington and coworkers seeks to relate an experimentally derived stagnation pressure to the vapor pressure of refractory materials. The stagnation pressure is determined by measuring the geometry of the free-jet expansions from laser-vaporized surfaces and employing a semi-empirical relationship which relates the measured geometry to the stagnation pressure of the flow and the ambient pressure. In Ref. 25, it was assumed that the vapor pressure of the material is equal to the stagnation pressure derived from the experimental data. Carbon vapor pressures determined in this manner were shown to agree reasonably well with those obtained from JANNAF¹³ thermochemical property data at measured surface temperatures.

²⁴

Covington, A., "Ames Free-jet Laser Vaporization Experiments," Data Report, NASA Ames Research Center, Mountain View, Calif., Sept. 1980.

²⁵

Covington, M.A., G.N. Liu, and K.A. Lincoln, "Free-jet Expansions from Laser-vaporized Planar Surfaces," AIAA Journal, 15, Aug. 1977, pp. 1174-1179.

Additional analysis of these experiments by Baker and Crowell⁵ indicated possible carbon melting at about 4250°K, and also showed that interpretation of the data in terms of JANNAF properties is not unique, i.e., other thermochemical data^{15,16} also are able to predict the measured data. The primary objectives of the new tests carried out this past year have been to uniquely determine the correct thermochemical property data (vapor pressure) and to establish the melt temperature and carbon species vaporization coefficients². Progress toward meeting these objectives is summarized below.

2. New Data Summary

New pulsed laser data obtained this year, as reported in Ref. 24, are summarized in Figs. 27 through 29. Over 100 new data points were obtained, with approximately two-thirds of these being for PG samples and the remainder for Graphnol. A few new data points also were obtained for ATJ-S graphite samples.

The PG data are shown in Fig. 27. For each data point, the peak total (stagnation) pressure, as deduced from the measured geometry of the free-jet expansion, is plotted versus the measured peak surface temperature. Experimental data obtained for Graphnol samples and new (1980) and old (1976) ATJ-S samples are given in Figs. 28 and 29. In Fig. 28, the total pressures derived from the free-jet geometry measurements are shown as a function of peak laser flux (power density). Reasonable agreement is seen between the new and the old ATJ-S graphite data points as well as between all three different types of carbon at a given value of \dot{q}_{max} . The divergence of the PG data from the ATJ-S and Graphnol data below $\dot{q}_{max} = 5 \times 10^5 \text{ W/cm}^2$ is due to the power density being too low to bring the sample up to the steady-state ablation temperature in the ATJ-S and Graphnol cases, whereas the much lower PG thermal conductivity (perpendicular to c-face) resulted in the PG reaching the ablation temperature during the laser pulse time.

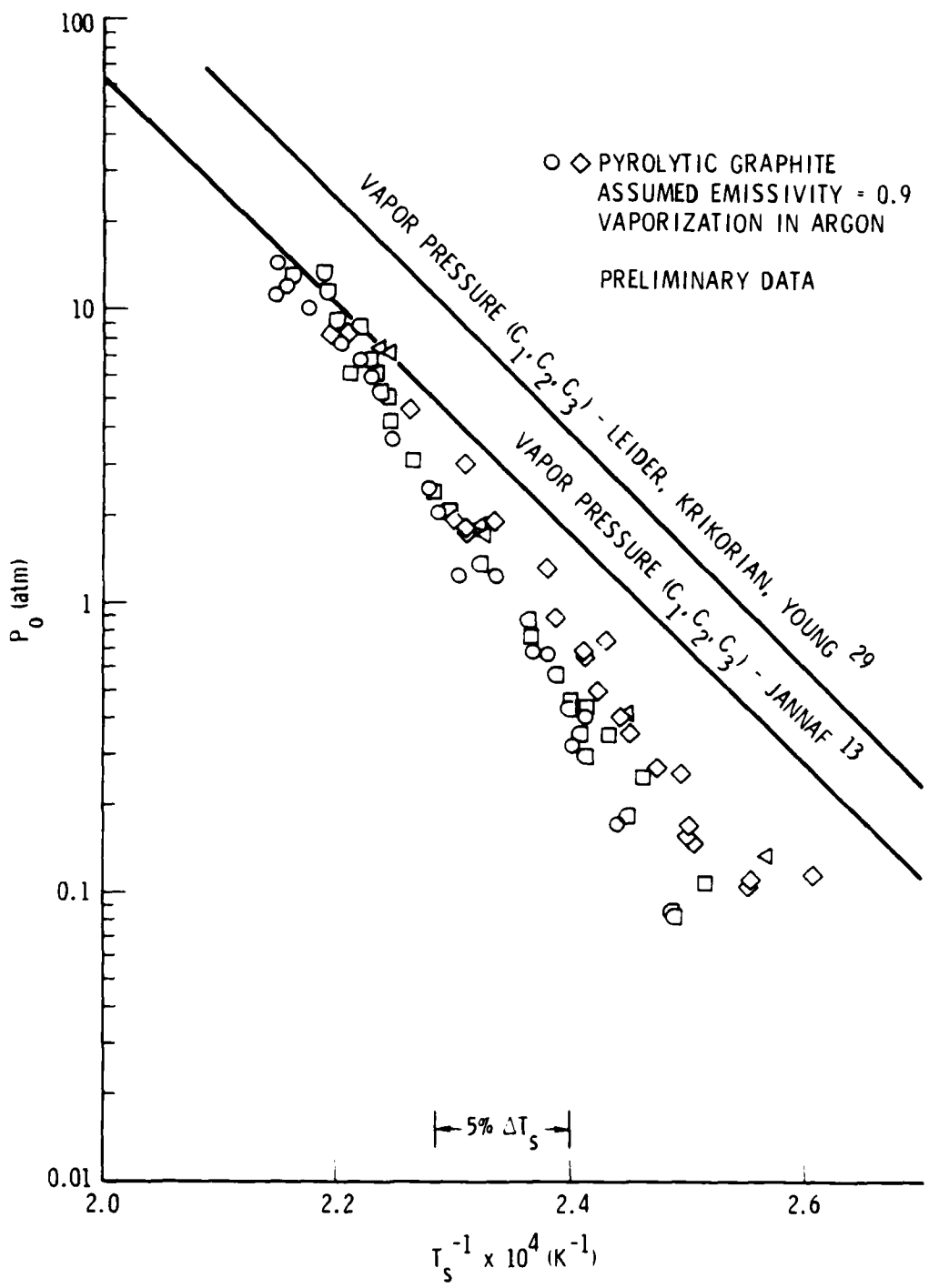


Fig. 27. Free-Jet Peak Total Pressure versus Peak Surface Temperature

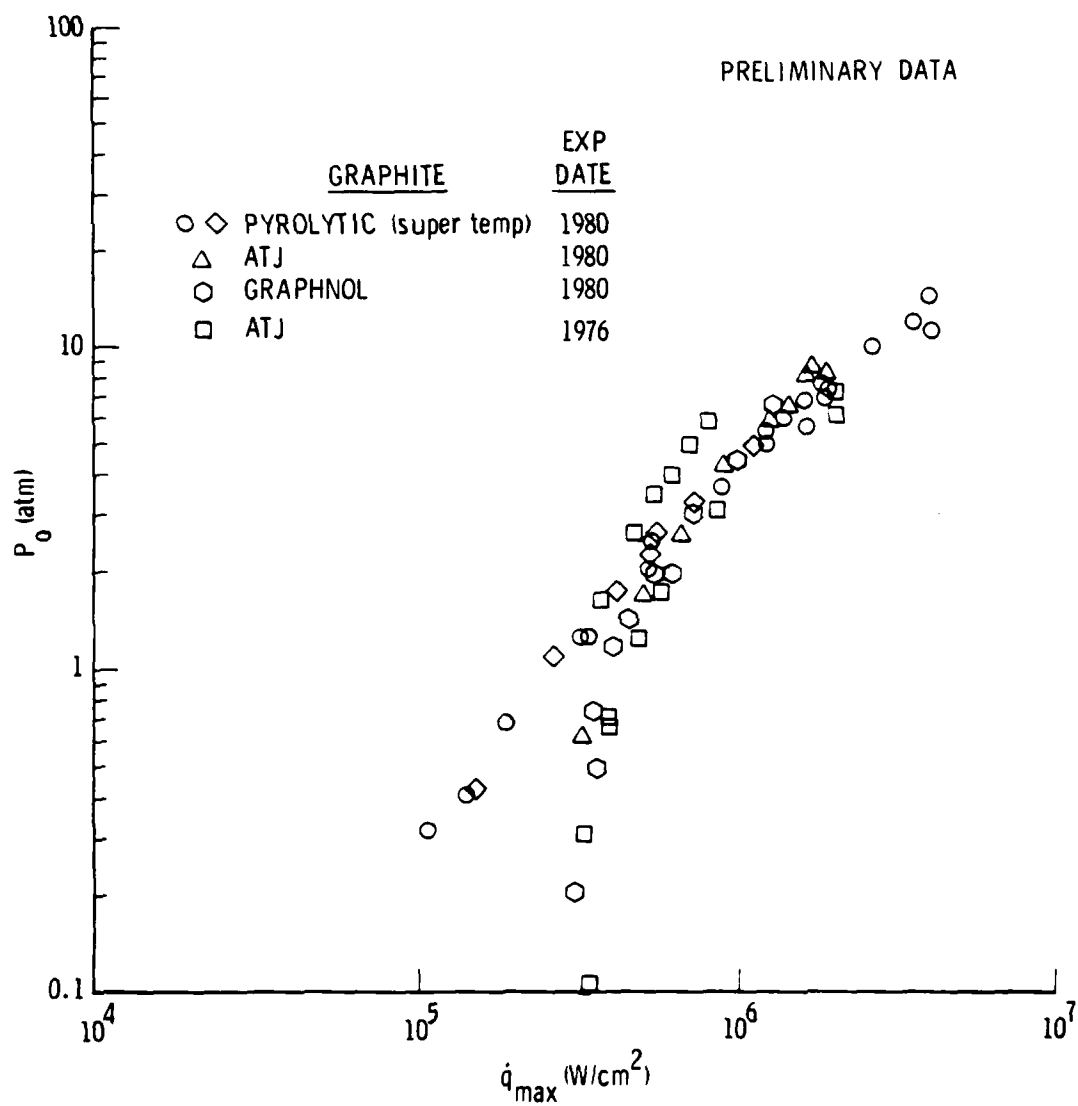


Fig. 28. Derived Free-Jet Total Pressure versus Peak Laser Flux for Vaporization in Argon

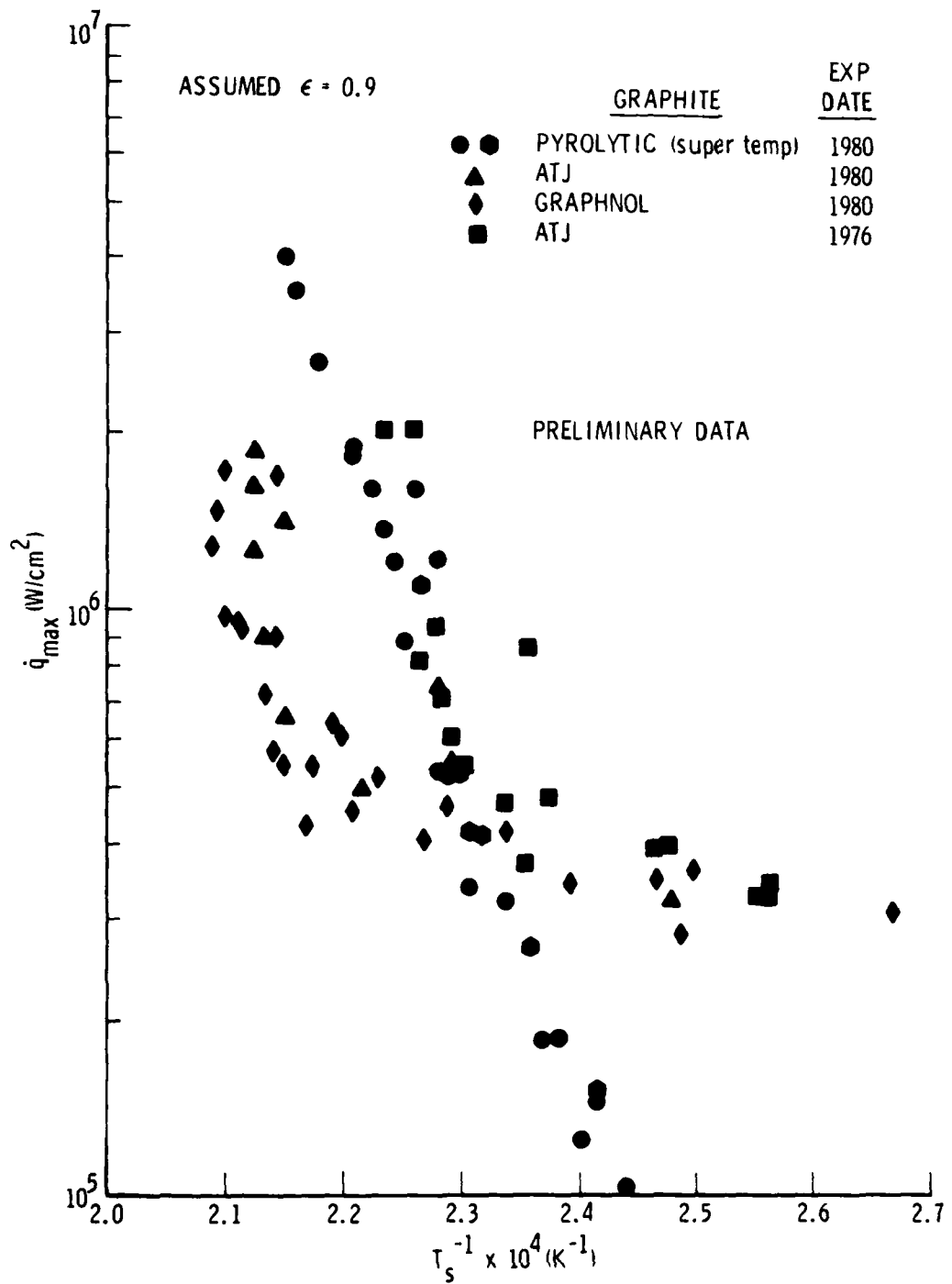


Fig. 29. Peak Surface Temperature versus Peak Laser Flux for Vaporization in Argon

In Fig. 29, the measured surface temperatures for the data points in Fig. 28 are shown for the various peak laser flux levels. The large differences in the data for inverse temperatures ($T_s^{-1} \times 10^4$, K $^{-1}$) greater than 2.3 again are due to thermal conductivity differences which result in different measured peak temperatures when \dot{q}_{max} is below about 5×10^5 W/cm 2 . However, for inverse temperatures less than 2.3, other differences not attributable to thermal conductivity are seen. First, the new and the old ATJ-S data are not in agreement. Also, the new ATJ-S and Graphnol data group together but are not in agreement with the PG data. A preliminary analysis of these results is given in Subsection V-D.

B. Surface Reflectance Measurements and Spectroscopy

Surface reflectance measurements, using an auxiliary laser, have been shown to give a good indication of surface melting associated with pulsed laser annealing of semiconductors²⁶. Significant progress has been made this year toward using this technique to detect the presence of a thin melt layer on an ablating carbon surface. The auxiliary laser and associated detection equipment have been purchased and put into place, and initial measurements are expected to be made in the fall of 1980²⁷.

A detailed evaluation of pulsed laser experimental data will require carbon species concentration measurements in addition to the stagnation pressure and surface temperature data as given in Figs. 27 through 29. By comparison of experimentally determined carbon species ratios with predictions for assumed frozen and equilibrium kinetics in the Knudsen layer (see Subsection III-C), a scaling relationship for the appropriate use of these

²⁶

Auston, D.H., et al., "Time Resolved Reflectivity of Ion-implanted Silicon During Laser Annealing," Appl. Phys. Lett., 33, 1978, pp. 437-440.

²⁷

Covington, M.A., Personal Communication, NASA Ames Research Center, Moffett Field, Calif.

bounding cases for the prediction of carbon vaporization at low pressures under high thermal radiation fluxes can be determined. Toward this end, initial spectroscopic data of the type intended to be used to determine the desired carbon species ratios are shown in Fig. 30 (from Ref. 24). The measured relative intensity levels of the carbon species C_3 (Swing band) emission spectrum ($\lambda = 3850 - 4200 \text{ \AA}$) and the C_2 (Swan band) emission spectrum ($\lambda = 5050 - 5200 \text{ \AA}$) are compared with predicted results from a synthesized band spectra computer program²⁸. We plan to obtain additional data of this type in the coming year.

C. Thulium Vaporization Experiments

These experiments²⁴ were undertaken to test the validity of the method being used to deduce carbon vapor pressure information from laser-induced free-jet expansions for a material which (a) vaporizes as a monatomic gas, (b) is very likely to have a unit vaporization coefficient, and (c) has established thermochemical data (vapor pressure information). Thus, the original model of Anisimov¹⁴ is applicable to such data without the further complicating factors (see Subsection III-C) of internal degrees of freedom of the molecules (polyatomic gases), nonunit vaporization coefficients, and several polyatomic species in the vapor with potential chemical reactions, i.e., the carbon system.

The element thulium was selected because it was desirable to have a material with a high melt temperature and significant vapor pressure at temperatures just below the melting point. These criteria were an attempt to ensure visible emission from the laser-vaporized plume so that it could be photographed to determine its geometry, sublimation of the material to avoid the complications of a melt layer and, finally, sufficiently high mass loss rates to have a measurable mass loss. Thulium melts at about 1800°K and

²⁸

Arnold, J.E., et al., "Line-by-line Transport Calculations for Jupiter Entry Probes," Progress in Astronautics and Aeronautics: Entry Heating and Thermal Protection, 69, W. OIstad (ed.), AIAA, New York, 1980, pp. 52-82.

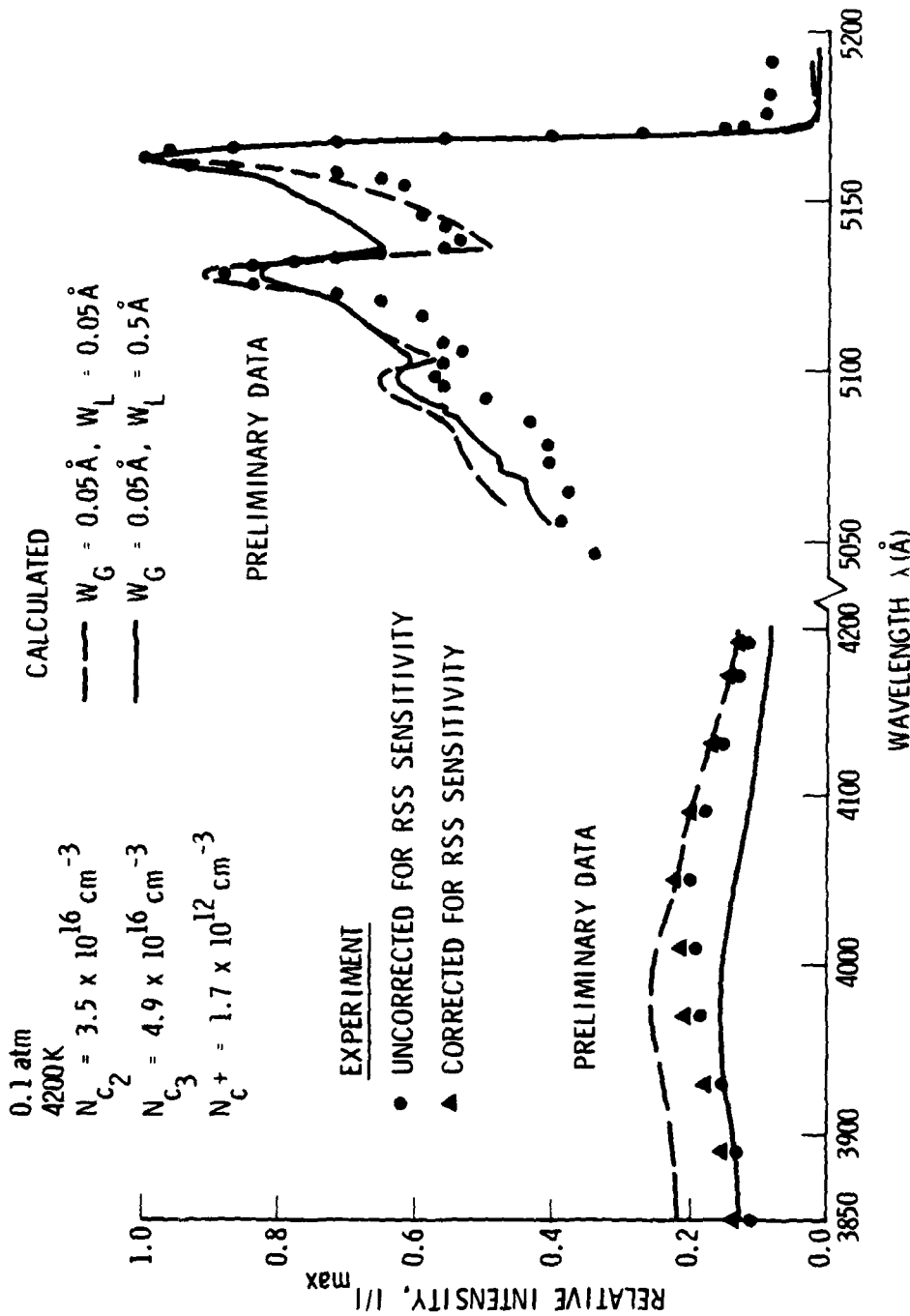


Fig. 30. Comparison of Calculated and Experimental Spectra-- C_2 ($\Delta v = 0$) and C_3

attains a vapor pressure greater than 250 torr before it melts. It was clearly the best of readily available materials with the desired properties.

Calculations and later experimental data revealed that with the pulsed laser available, the thulium could not be brought up to a steady-state ablation temperature in the pulse time available at a power density (laser flux) low enough to not melt the surface. A representative picture of a laser-induced plume from the surface of a flat thulium test sample is shown in Fig. 31. In this picture, and many others taken at different laser flux levels, ambient chamber pressures, and camera exposure times, the Mach disc location needed to deduce plume total pressures could not be seen. Significant absorption and emission from induced fluorescence of the thulium atoms is taking place, but this obscures any details of the free-jet flow patterns and also tends to overshadow the continuum radiation from the hot vaporizing surface which is used to determine ablation temperatures.

While the above results did not give the desired data for verifying the modeling and data analysis procedures, additional measurements by Lincoln²⁴ with a time-of-flight mass spectrometer verified that the major species in the laser-induced plume is monatomic thulium. Thus, thulium still represents a good candidate material for model verification if an independent method of determining the mass loss rate can be found. One possibility would be to conduct CW laser tests as described in Section IV and to weigh the samples before and after exposure. Approximate calculations indicate that lower laser beam power densities and longer run times would facilitate obtaining data below the thulium melt temperature.

D. PRELIMINARY DATA ANALYSIS

This discussion is primarily limited to the new PG data shown in Fig. 27. The sensitivity analysis performed with the nonlinear multiple carbon species Knudsen layer model, as discussed in Subsection III-C, clearly shows

Peak Laser Flux: 2.0×10^5 W/cm²
Laser Pulse Length: ~700 μ sec
Laser Beam Diameter: 2.4 mm
Beam Incident Angle: 25°
Ambient Gas: Argon
Ambient Pressure: 3.1 torr
Surface Temperature: > 2000K



Fig. 31. Self-Luminous Monatomic Thulium Vapor Plume
Created by Laser Heating

that carbon vapor pressure and vaporization coefficient information cannot be unambiguously obtained from data in which the flow at the edge of the Knudsen layer is always sonic. All the data in Fig. 27 fit into this category. Thus, the final interpretation of these data will need to be done in conjunction with the Section IV CW laser data which do not have this limitation.

It is important and significant, however, to realize that the data in Fig. 27 cover measured surface temperatures from about 3850^0K up to greater than 4700^0K . In the temperature range from 3850 to 4000^0K , overlapping data from both the CW and pulsed laser tests are available. This provides the link required for unique determination of vapor pressures and vaporization coefficients. Since most experimentally determined melt temperatures lie between 4000 and 4400^0K , the surface reflectivity measurements to be performed this fall to look for surface melting will aid considerably in the detailed interpretation of data up to 4700^0K . It is possible that melting phenomena are associated with some of the anomalies of the Fig. 29 data.

While published experimental data indicate melting at least at temperatures above 4400^0K , the theoretical calculations of Ref. 29 predict a melt temperature of 4765^0K . If we assume no melting, even at 4700^0K , what do the Fig. 27 data indicate? First of all, the slope of the data is not parallel either to the JANNAF or the Ref. 29 predicted vapor pressures. From the analysis of Subsection III-C, it can easily be shown that for these experiments the vapor pressure is proportional to the measured stagnation pressure. Thus, the data should be parallel to the vapor pressure curves unless a strongly temperature-dependent vaporization coefficient alters the p^0 versus $1/T_s$ behavior. An example of such behavior predicted, with vaporization coefficient a strong function of temperature, is shown in Fig. 32.

29

Leider, H.R., O.H. Krikorian, and D.A. Young, "Thermodynamic Properties of Carbon Up to the Critical Point," Carbon, 11, 1973, pp. 555-563.

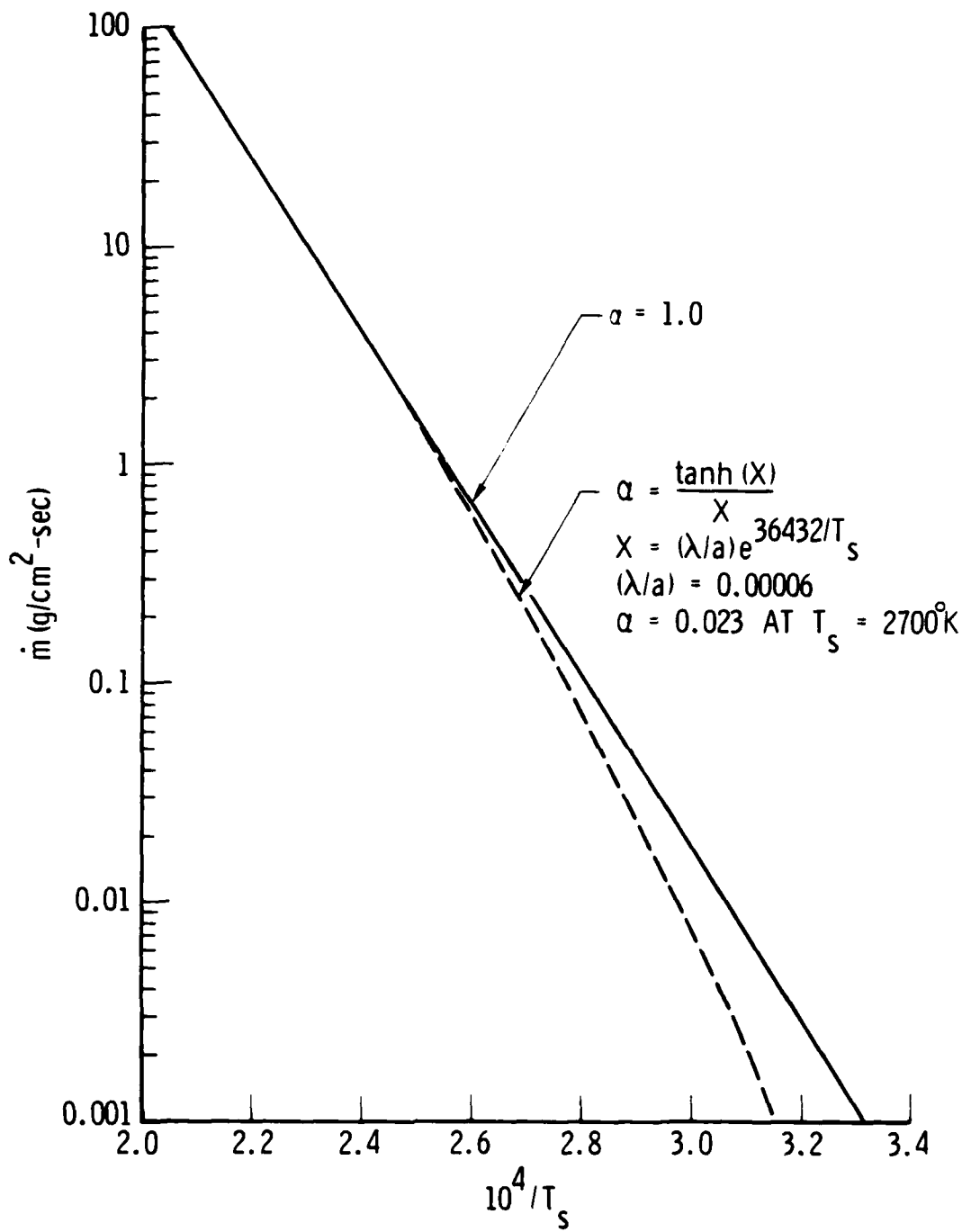


Fig. 32. Dependence of Mass Loss Rate on Vaporization Coefficient and T_s

Even with the carbon species C₃ vaporization coefficient decreased to its experimentally determined value of 0.023 at 2700°K and increasing to 1.0 at high temperatures (a strong temperature dependence), the predicted mass loss rates do not fall off at lower temperatures as rapidly as the data in Fig. 27 would seem to indicate. Thus, other possible causes of this behavior, including chemical reactions or condensation occurring in the plume and affecting the measured Mach disc location measurements, are being investigated.

VI. CARBON MELT TEMPERATURE

Controversy concerning the melt temperature of carbon has had a long history³⁰. While most recent experimental work concerning the triple point of carbon³¹⁻³⁴ has been interpreted as indicating a triple-point (melt) temperature somewhere between 4000 and 4400°K, it has been argued that other experimental data indicate a triple-point temperature near 3800°K¹⁹. The corresponding triple-point pressures are argued to be near 100 atm for the higher temperature triple points and about 0.2 atm for the 3800°K triple point.

Resolution of this very large (600°K) uncertainty in the melt temperature of carbon is one of the primary objectives of the work presented in this report^{1,2}. A unique opportunity to do this is afforded because the CW laser experiments discussed in Section IV were carried out using the same laser and essentially the same apparatus and instrumentation as that of the reported 3800°K triple-point experiments¹⁹. The importance of resolving this uncertainty, in addition to the desirability of accurate knowledge of basic thermochemical properties, is dictated by potentially very substantial loss of the energy-dissipating efficiency of carbon materials upon the onset of melting³⁻⁵.

³⁰

Whittaker, A.G., "The Controversial Carbon Solid-Liquid-Vapor Triple Point," Nature, 276(5689), 14 Dec. 1978, pp. 695-696.

³¹

Noda, T. and M. Inagaki, Bull. Chem. Soc. Japan, 37, 1964, p. 1710.

³²

Fateeva, N.S., L.F. Vereshchagin, and V.S. Kolotygin, Sov. Phys. Dokl., 8, 1964, pp. 893-903.

³³

Schoessow, G.J., "Graphite Triple Point and Solidus-liquidus Interface Experimentally Determined Up to 1000 Atmospheres," Phys. Rev. Lett., 21, 1968, p. 738.

³⁴

Gokcen, N.A., et al., "Determination of Graphite/Liquid/Vapor Triple Point by Laser Heating," High Temperature Science, 8, June 1976, pp. 81-97.

We are approaching work which is directed toward final accurate determination of the melt temperature in two phases. The first phase, discussed here, is to place the melt temperature in one of three temperature ranges: near 3800°K , $4000\text{-}4400^{\circ}\text{K}$, or greater than 4400°K . There apparently are no experimental data which indicate a triple-point temperature in the highest temperature range (see below). The excellent review paper by Palmer and Shelef concludes that "it seems very probable that it (the triple point) lies at about 100 atm and $4600\text{-}4800$ K." The experimental data reviewed by Palmer and Shelef, however, include only one data point above 4600°K , the triple-point temperature of 4670°K reported by Fateeva, et al.³⁴. Haaland³⁵ has pointed out that this temperature was later corrected downward to 4040°K ³⁶ because of improper pyrometer filter corrections used in the earlier work.

Theoretical calculations of Leider, Krikorian, and Young²⁹, based upon the carbon species C_1 through C_7 , thermochemical data of Lee and Sanborn¹⁷, predict a triple-point temperature of 4765°K . Theoretical calculations based upon the JANNAF thermochemical data¹³, which only considers carbon species C_1 through C_5 , predict a triple-point temperature of about 4900°K . The theoretical calculations do not consider the possibility of phase changes in solid carbon at high temperature²². Thus, in summation, some experimental data are interpreted to show carbon melting near 3800°K , most experimental data seem to indicate a melt temperature of $4000\text{-}4400^{\circ}\text{K}$, and recent theoretical calculations predict $T_{\text{melt}} > 4400^{\circ}\text{K}$.

At the present time, it is tentatively concluded that the melt temperature lies in the $4000\text{-}4400^{\circ}\text{K}$ range. This conclusion is based upon (a) the weight of the evidence given by a large fraction of the carbon triple-point experimental data, and (b) a preliminary comparison of high-speed motion

³⁵

Haaland, D.M., "Graphite-Liquid-Vapor Triple Point Pressure and the Density of Liquid Carbon," Carbon, 14, 1976, pp. 357-361.

³⁶

Vershchagin, L.F. and N.S. Fateeva, Sov. Phys. JETP, 28, 1969, p. 597.

AD-PAS10 589 AEROSPACE CORP. EL SEGUNDO CA VEHICLE ENGINEERING DIV
CARBON NONEQUILIBRIUM PHASE CHANGE. (U)
DEC 81 R L BAKER

UNCLASSIFIED TR-0082(2728-02)-1

F/0 7/4

F04701-81-C-0082

ML

SD-TR-81-89

2nd 2
A. Baker



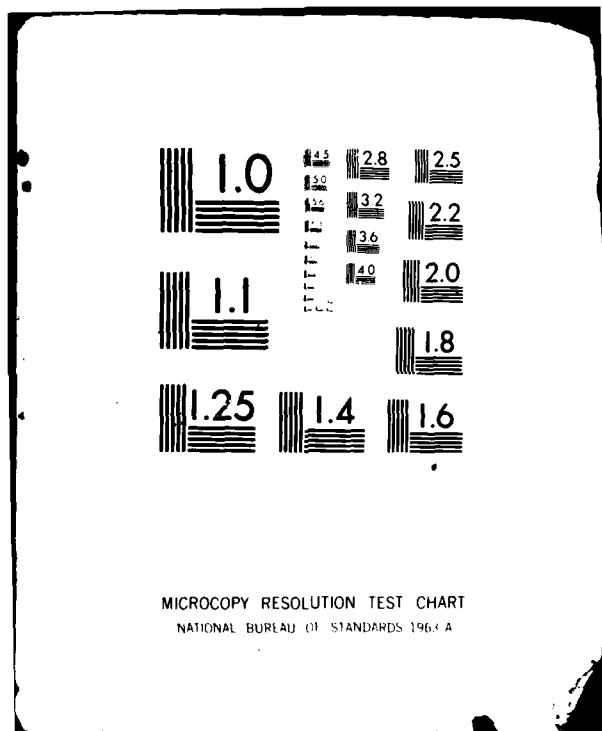
END

DATA

FILED

10-82

RTIC



pictures, obtained as part of the CW laser tests described in Section IV, with the high-speed film coverage of similar tests which has been interpreted as showing evidence of melting at 3800°K by Whittaker, et al.¹⁹. None of the most recent films shows large "liquid" carbon globules, as seen coming off the rapidly spinning sample in the earlier film of Whittaker and coworkers, even though ten films were obtained at temperatures above 3800°K including one for a measured temperature of 3965°K . Thus, the evidence for melting based upon seeing large "liquid" carbon globules is not repeatable. This could be due to a number of experimental difficulties²¹ or for other reasons as discussed below.

It is acknowledged that other consistently occurring evidence is given in Ref. 19 to support the claim of melting. This evidence includes spherules apparently solidified from liquid carbon and splats on flat surfaces interpreted as being caused by liquid carbon spheres impacting the solid surface. A potential explanation of these is that they result from nonequilibrium condensation of carbyne liquid drops from carbon vapor. It remains to explain what was actually seen in the earlier film, interpreted as being large "liquid" carbon globules, and not seen in many subsequent films. It is possible, based upon the recent films, that it was pockets of high temperature carbon vapor which would have a viscosity much higher than that of the surrounding chamber gas. The reason this behavior has not been seen again could be related to an unstable ablating carbon vapor plume at the surface of the cylindrical sample. The instability may have been unique to that one particular run because of the highly irregular and nonuniform ablation of the pyrolytic graphite evidenced in the post-test appearance of the sample. This interpretation is being investigated further.

Presuming that our tentative conclusion concerning a $4000\text{-}4400^{\circ}\text{K}$ melt temperature can be substantiated, attention will then be focused upon detailed interpretation of all the laser ablation data obtained this past year. New pulsed laser tests planned for the fall of 1980²⁷, which will employ an

auxiliary laser to indicate surface melting by detection of the substantial change in reflectance upon melting, are expected to play a key role in the final determination of melt temperature. This technique has been very successfully demonstrated for detecting surface melting in the thermal annealing of semiconductors²⁶. In addition, we will be continuing discussions with Dr. Ared Cezairliyan of the National Bureau of Standards in Washington, D.C., who is planning to carry out new conventional triple-point measurements for carbon³⁷.

³⁷

Cezairliyan, A., Personal Communication, National Bureau of Standards, Washington, D.C., Apr. 1980.

REFERENCES

1. "Proposal to Perform a Carbon Nonequilibrium Phase Change Research Program," The Aerospace Corporation, El Segundo, Calif., Apr. 1979.
2. "Proposal to Continue the Carbon Nonequilibrium Phase Change Research Program," The Aerospace Corporation, El Segundo, Calif., Aug. 1979.
3. Baker, R.L., "An Irreversible Thermodynamics Model for Graphite Sublimation in Radiation Environments," Progress in Astronautics and Aeronautics: Outer Planet Heating and Thermal Protection Systems, 64, R. Viskanta (ed.), AIAA, New York, 1979, pp. 210-227.
4. Baker, R.L. and P.G. Crowell, "Graphite Material Ablation Performance in High Thermal Radiation Environments," Progress in Astronautics and Aeronautics: Entry Heating and Thermal Protection, 69, W. OIstad (ed.), AIAA, New York, 1980, pp. 198-221.
5. Baker, R.L., "Graphite Sublimation Chemistry Nonequilibrium Effects," AIAA Journal, 15, Oct. 1977, pp. 1391-1397.
6. Landau, H.G., "Heat Conduction in a Melting Solid," Quart. Appl. Phys., 36, Feb. 1965, pp. 462-468.
7. Crowell, P.G., "The Nonequilibrium Ablation of Carbon," Report No. TOR-0079(4550-76)-1, The Aerospace Corporation, El Segundo, Calif., Nov. 1978.
8. Dabby, F.W. and U.-C. Paek, "High-intensity Laser Induced Vaporization and Explosion of Solid Material," IEEE J. of Quantum Electronics, QE-8(2), Feb. 1972, pp. 106-111.
9. Ytrehus, T., "Theory and Experiments on Gas Kinetics in Evaporation," Progress in Astronautics and Aeronautics: Rarefied Gas Dynamics, 51(II), J.L. Potter (ed.), AIAA, New York, 1977, pp. 1197-1212.
10. Knight, C.J., "Theoretical Modeling of Rapid Surface Vaporization with Back-Pressure," AIAA J., 17, May 1979, pp. 519-523.
11. Weichert, H., "Boundary Conditions for the Liquid-Vapor Interface of Helium II," J. Phys. C: Solid State Phys., 9, 1976, pp. 553-569.
12. Bornhorst, W.J. and G.N. Hatsopoulos, "Analysis of a Phase Change by the Methods of Irreversible Thermodynamics," Journal of Applied Mechanics, 34, Dec. 1967, pp. 840-846.
13. JANNAF Thermochemical Tables, National Bureau of Standards, NBS-37, June 1971.

REFERENCES (Continued)

14. Anisimov, S.I., "Vaporization of Metal Absorbing Laser Radiation," Soviet Physics JETP, 27(1), 1968, pp. 182-183.
15. Kratsch, K.M., et al., "Graphite Ablation in High Pressure Environments," AIAA Paper 68-1153, 1968.
16. Dolton, T.A., H.E. Goldstein, and R.E. Mauer, "Thermodynamic Performance of Carbon in Hyperthermal Environments," Progress in Astronautics and Aeronautics: Thermal Design Principles of Spacecraft and Entry Bodies, 21, J.T. Bevans (ed.), AIAA, New York, 1969, pp. 169-201.
17. Lee, E.L. and R.H. Sanborn, "Extended and Improved Thermal Functions for the Gaseous Carbon Species C₁-C₇ from 298 to 10000 K," High Temperature Science, 5, 1973, pp. 438-453.
18. Rosenblatt, G., Personal Communication, Department of Chemistry, Pennsylvania State University, University Park, Pa., Dec. 1979.
19. Whittaker, A.G., et al., "Carbon Vapor Pressure in the Range 3450-4500 K and Evidence for Melting at ~3800 K," to be submitted to High Temperature Science.
20. Whittaker, A.G., et al., "System Employing Laser Heating for the Measurement of High-temperature Properties of Materials over a Wide Pressure Range," Review of Scientific Instruments, 48(6), June 1972, pp. 632-639.
21. Whittaker, A., Personal Communication, The Aerospace Corporation, El Segundo, Calif.
22. Whittaker, A.G., "Carbon: A New View of Its High-Temperature Behavior," Science, 20, 19 May 1978, pp. 763-764.
23. Doak, R.B. and J.R. Baron, "Activation Studies in Graphite Oxidation," Progress in Astronautics and Aeronautics: Rarefied Gas Dynamics, 51(II), J.L. Potter (ed.), AIAA, New York, 1977, pp. 621-634.
24. Covington, A., "Ames Free-jet Laser Vaporization Experiments," Data Report, NASA Ames Research Center, Mountain View, Calif., Sept. 1980.
25. Covington, M.A., G.N. Liu, and K.A. Lincoln, "Free-jet Expansions from Laser-vaporized Planar Surfaces," AIAA Journal, 15, Aug. 1977, pp. 1174-1179.
26. Auston, D.H., et al., "Time Resolved Reflectivity of Ion-implanted Silicon During Laser Annealing," Appl. Phys. Lett., 33, 1978, pp. 437-440.

REFERENCES (Concluded)

27. Covington, M.A., Personal Communication, NASA Ames Research Center, Moffett Field, Calif.
28. Arnold, J.O., et al., "Line-by-line Transport Calculations for Jupiter Entry Probes," Progress in Astronautics and Aeronautics: Entry Heating and Thermal Protection, 69, W. OIstad (ed.), AIAA, New York, 1980, pp. 52-82.
29. Leider, H.R., O.H. Krikorian, and D.A. Young, "Thermodynamic Properties of Carbon Up to the Critical Point," Carbon, 11, 1973, pp. 555-563.
30. Whittaker, A.G., "The Controversial Carbon Solid-Liquid-Vapor Triple Point," Nature, 276(5689), 14 Dec. 1978, pp. 695-696.
31. Noda, T. and M. Inagaki, Bull. Chem. Soc. Japan, 37, 1964, p. 1710.
32. Fateeva, N.S., L.F. Vereshchagin, and V.S. Kolotygin, Sov. Phys. Dokl., 8, 1964, pp. 893-903.
33. Schoessow, G.J., "Graphite Triple Point and Solidus-liquidus Interface Experimentally Determined Up to 1000 Atmospheres," Phys. Rev. Lett., 21, 1968, p. 738.
34. Gokcen, N.A., et al., "Determination of Graphite/Liquid/Vapor Triple Point by Laser Heating," High Temperature Science, 8, June 1976, pp. 81-97.
35. Haaland, D.M., "Graphite-Liquid-Vapor Triple Point Pressure and the Density of Liquid Carbon," Carbon, 14, 1976, pp. 357-361.
36. Vershchagin, L.F. and N.S. Fateeva, Sov. Phys. JETP, 28, 1969, p. 597.
37. Cezairliyan, A., Personal Communication, National Bureau of Standards, Washington, D.C., Apr. 1980.

